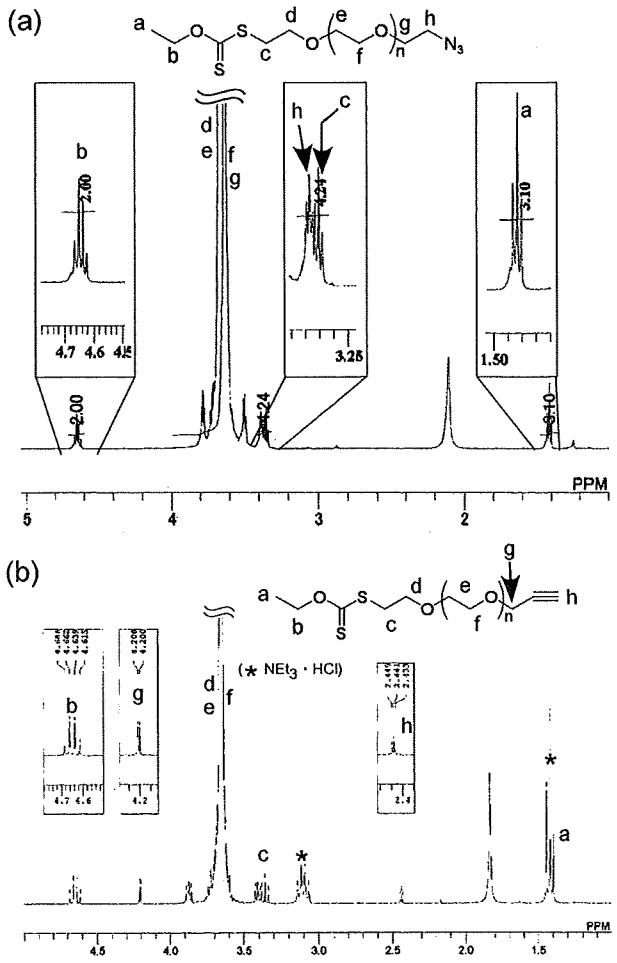

Figure 5. ^{1}H NMR spectra of derivatized samples with dithiocarbonate moiety: Azide-PEG (a) (500 MHz in $CDCl_3$) and Alkyne-PEG (b) (300 MHz in $CDCl_3$).

Alkyne), the derivatization of the α-terminal end to the thiol functional group was examined after the removal of the THP protective group. PEG derivatives introduced with the dithiocarbonate moiety at the α-position were prepared as the first step to HS-PEG-Y (Y = Azide and Alkyne) through the two-step modification, the mesylation and the substitution by potassium xanthogenate, of hydroxyl function as described in the Experimental Section. In the ^{1}H NMR spectrum (Figure 5a), the characteristic methyl and methylene signals of the dithiocarbonate unit were clearly observed at 1.85 (S(C=S)−OCH$_2$C$\underline{H}_3$), and 4.65 ppm (S(C=S)O−C$\underline{H}_2$CH$_3$), respectively, and the proton signal assigned to the azido group (-C$\underline{H}_2$N$_3$: δ = 3.37 ppm) was also detected. In addition, comparison between the integral ratios of these signals indicated the quantitative conversion of the hydroxyl group to the dithiocarbonate structure without any damage on the azido functionality. For derivatization of HO-PEG-Alkyne, the reaction similar to the azido-terminated PEG sample was conducted. From the ^{1}H NMR analysis of the resultant polymer, both signals assigned to the alkyne moiety (C$\underline{H}$ of Alkyne: δ = 2.41 ppm and O-C$\underline{H}_2$-C of Alkyne: 4.18 ppm) and the dithiocarbobnate structure (S(C=S)−OCH$_2$C$\underline{H}_3$): δ = 1.85 and S(C=S)O−C$\underline{H}_2$CH$_3$): δ = 4.65 ppm) were clearly detected (Figure 5b). These results indicate the successful derivatization of heterobifunctional THP-PEG-Y (Y = Azide and Alkyne) with dithiocarbonate moiety under the mild reaction condition. Figure 6 shows the ^{1}H NMR spectrum of the obtained HS-PEG-Azide. The proton signals corresponding to the ethyldithiocarbonate moiety completely disappeared, while the characteristic signals of both azide and methylene proton adjacent to thiol group were detected (CH$_2$C$\underline{H}_2$N$_3$: δ 3.39, and CH$_2$C$\underline{H}_2$S: δ 2.89 ppm, respectively). In addition, no decomposition of the azido group during the alkali reaction was detected in the ^{1}H NMR spectrum, suggesting the end-functionalization with the high reaction conversion. After the thiolation reaction of alkyne-terminated PEG, the characteristic signals were observed without any side reaction (see the Experimental Section). These investigations indicated that the thiolation reaction of PEGs possessing azido or alkyne function proceeded under the mild conditions.

In conclusion, the facile synthesis of the azido- or alkyne-possessing heterobifunctional PEGs via EO polymerization was demonstrated in this study. Controlling the MW and the selective functionalization of the α- and ω-termini of heterobifunctional PEGs was successfully presented. These functional PEG derivatives can be used in Cu(I)-catalyzed 1,3-dipolar cycloaddition reaction (click chemistry) to introduce versatile biofunctional moieties into the azido or alkyne terminus, and are thus relevant to a wide range of applications in the field of bioconjugate chemistry.

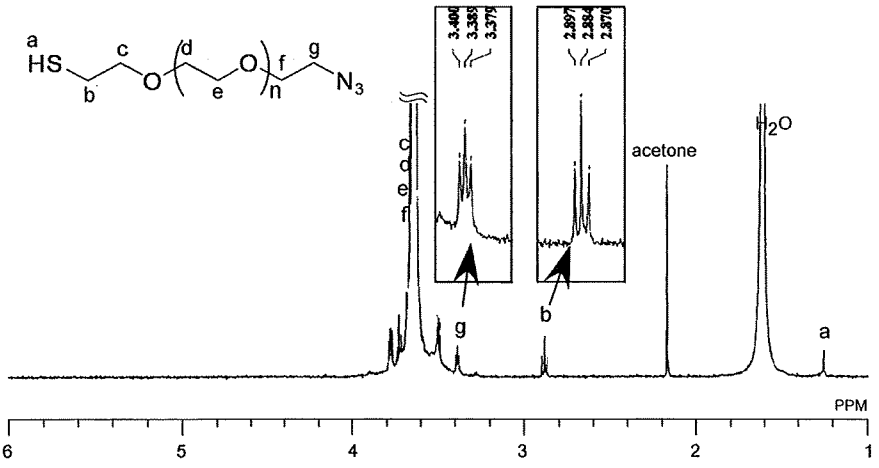

Figure 6. 500 MHz ^{1}H NMR spectrum of HS-PEG-Azide (in $CDCl_3$).

ACKNOWLEDGMENT

This work was supported by the Core Research for Evolutional Science and Technology (CREST) from the Japan Science and Technology Agency (JST).

Supporting Information Available: MALDI-TOF MS spectra of THP-PEG-OH and THP-PEG-N_3. This material is available free of charge via the Internet at http://pubs.acs.org.

LITERATURE CITED

(1) Beddard, G. S., and West, M. A., Eds. (1981) *Fluorescent Probes*, Academic Press, London.
(2) Kraayenhof, R., Visser, A. J. W. G.; and Gerritsen, H. C. (2002) *Fluorescence Spectroscopy, Imaging and Probes: New Tools in Chemical, Physical and Life Sciences (Springer Series on Fluorescence, 2)*, Springer-Verlag, Berlin.
(3) Abuchowski, A., McCoy, J. R., Palczuk, N. C., Van Es, T., and Davis, F. F. (1977) Effect of covalent attachment of polyethylene glycol on immunogenicity and circulating life of bovine liver catalase. *J. Biol. Chem. 252*, 3582–3586.
(4) Harris, J. M., Ed. (1992) *Poly(ethylene glycol) Chemistry: Biotechnical and Biomedical Applications*, Plenum Press, New York.
(5) Roberts, M. J., Bentley, M. D., and Harris, J. M. (2002) Chemistry for peptide and protein PEGylation. *Adv. Drug Delivery Rev. 54*, 459–476.
(6) Katre, N. V. (1993) The conjugation of proteins with polyethylene glycol and other polymers. Altering properties of proteins to enhance their therapeutic potential. *Adv. Drug Delivery Rev. 10*, 91–114.
(7) Graham, L. M. (2003) Pegaspargase: a review of clinical studies. *Adv. Drug Delivery Rev. 55*, 1293–1302.
(8) Duncan, R. (2003) The drawing era of polymer therapeutics. *Nat. Rev. Drug Discovery 2*, 347–360.
(9) Rostovtsev, V. V., Green, L. G., Fokin, V. V., and Sharpless, K. B. (2002) A stepwise Huisgen cycloaddition process: copper(I)-catalyzed regioselective "ligation" of azides and terminal alkynes. *Angew. Chem., Int. Ed. 41*, 2596–2599.
(10) Wang, Q., Chan, T. R., Hilgraf, R., Fokin, V. V., Sharpless, K. B., and Finn, M. G. (2003) Bioconjugation by copper(I)-catalyzed azide-alkyne [3 + 2] cycloaddition. *J. Am. Chem. Soc. 125*, 3192–3193.
(11) Lutz, J. F. (2007) 1,3-Dipolar cycloadditions of azides and alkynes: A universal ligation tool in polymer and materials science. *Angew. Chem., Int. Ed. 46*, 1018–1025.
(12) Link, A. J., and Tirrell, D. A. (2003) Cell surface labeling of *Escherichia coli* via copper(I)-catalyzed [3 + 2] cycloaddition. *J. Am. Chem. Soc. 125*, 11164–11165.
(13) Deiters, A., Cropp, T. A., Mukherji, M., Chin, J. W., Anderson, J. C., and Schultz, P. G. (2003) Adding amino acids with novel reactivity to the genetic code of *Saccharomyces cerevisiae*. *J. Am. Chem. Soc. 125*, 11782–11783.
(14) Lin, P. C., Ueng, S. H., Tseng, M. C., Ko, J., Huang, K. T., Yu, S. C., Adoak, A. K., Chen, Y. J., and Lin., C. C. (2006) Site-specific protein modification through Cu-catalyzed 1,2,3-triazole formation and its implementation in protein microarray fabrication. *Angew. Chem., Int. Ed. 45*, 4286–4290.
(15) Natarajan, A. (2007) Construction of di-scFv through a trivalent alkyne-aizde 1,3-dipolar cycloaddition. *Chem. Commun.* 695–697.
(16) Opsteen, J. A., and van Hest, J. C. M. (2005) Modular synthesis of block copolymers via cycloaddition of terminal azide and alkyne functionalized polymers. *Chem. Commun.* 57–59.
(17) Peng, S.-M., Chen, Y., Hua, C., and Dong, C.-M. (2009) Dendron-like polypeptide/linear poly(ethylene oxide) biohybrids with both asymmetrical and symmetrical topologies synthesized via the combination of click chemistry and ring-opening polymerization. *Macromolecules 42*, 104–113.
(18) Lee, S.-M., Chen, H., O'Halloran, T. V., and Nguyen, S. T. (2009) "Clickable" polymer-caged nanobins as a modular drug delivery platform. *J. Am. Chem. Soc. 131*, 9311–9320.
(19) Hiki, S., and Kataoka, K. (2007) A facile synthesis of azido-terminated heterobifunctional poly(ethylene glycol)s for "click" conjugation. *Bioconjugate Chem. 18*, 2191–2196.
(20) Wuts, P. G. M., and Greene, T. W. (2006) *Greene's Protective Groups in Organic Synthesis*, 4th ed.; John Wiley & Sons Inc.
(21) Szwarc, M., Levy, M., and Milkovich, R. (1956) Polymerization initiated by electron transfer to monomer. A new method of formation of block polymers. *J. Am. Chem. Soc. 78*, 2656.
(22) Akiyama, Y., Nagasaki, Y., and Kataoka, K. (2004) Synthesis of heterotelechelic poly(ethylene glycol) derivatives having α-benzaldehyde and ω-pyridyl disulfide groups by ring opening polymerization of ethylene oxide using 4-(diethoxymethyl)benzyl alkoxide as a novel initiator. *Bioconjugate Chem. 15*, 424–427.
(23) Zalipsky, S. (1995) Functionalized poly(ethylene glycol) for preparation of biologically relevant conjugates. *Bioconjugate Chem. 6*, 150–165.

BC900253P

NANOMEDICINE

Journal of Controlled Release 140 (2009) 306–311

Contents lists available at ScienceDirect

Journal of Controlled Release

journal homepage: www.elsevier.com/locate/jconrel

Enhanced magnetic resonance imaging of experimental pancreatic tumor *in vivo* by block copolymer-coated magnetite nanoparticles with TGF-β inhibitor

Michiaki Kumagai [a,e,1], Mitsunobu R. Kano [b,f,1], Yasuyuki Morishita [b], Motomi Ota [a], Yutaka Imai [a], Nobuhiro Nishiyama [a,e,f], Masaki Sekino [c], Shoogo Ueno [d], Kohei Miyazono [b,f], Kazunori Kataoka [a,e,f,*]

[a] Department of Materials Engineering, Graduate School of Engineering, The University of Tokyo, 7-3-1 Hongo, Bunkyo-ku, Tokyo 113-8656, Japan
[b] Department of Molecular Pathology, Graduate School of Medicine, The University of Tokyo, 7-3-1 Hongo, Bunkyo-ku Tokyo 113-0033, Japan
[c] Department of Advanced Energy, Graduate School of Frontier Sciences, The University of Tokyo, 5-1-5, Kashiwanoha, Kashiwa-shi, Chiba, 277-8561, Japan
[d] Department of Applied Quantum Physics, Graduate School of Engineering, Kyushu University, 6-10-1 Hakozaki, Higashi-ku Fukuoka 812-8581, Japan
[e] Center for Disease Biology and Integrative Medicine, School of Medicine, The University of Tokyo, 7-3-1 Hongo, Bunkyo-ku, Tokyo 113-0033, Japan
[f] Center for NanoBio Integration, The University of Tokyo, 7-3-1 Hongo, Bunkyo-ku, Tokyo 113-8656, Japan

ARTICLE INFO

Article history:
Received 13 March 2009
Accepted 5 June 2009
Available online 12 June 2009

Keyword:
Magnetic resonance imaging
Pancreatic cancer
TGF-β
Magnetite nanoparticles
Poly(ethylene glycol)

ABSTRACT

Early detection of solid tumors, particularly pancreatic cancer, is of substantial importance in clinics. Enhanced magnetic resonance imaging (MRI) with iron oxide nanoparticles is an available way to detect the cancer. The effective and selective accumulation of these nanoparticles in the tumor tissue is needed for improved imaging, and in this regard, their longevity in the blood circulation time is crucial. We developed here block copolymer-coated magnetite nanoparticles for pancreatic cancer imaging, by means of a chelation between the carboxylic acid groups in poly(ethylene glycol)–poly(aspartic acid) block copolymer (PEG–PAsp) and Fe on the surface of the iron oxide nanoparticles. These nanoparticles had considerably narrow distribution, even upon increased ionic strength or in the presence of fetal bovine serum. The PEG–PAsp-coated nanoparticles were further shown to be potent as a contrast agent for enhanced MRI for an experimental pancreatic cancer, xenografts of the human-derived BxPC3 cell line in BALB/c nude mice, with combined administration of TGF-β inhibitor. Iron staining of tumor tissue confirmed the accumulation of the nanoparticles in tumor tissue. Use of the PEG–PAsp-coated magnetite nanoparticles, combined with the TGF-β inhibitor, is of promising clinical importance for the detection of intractable solid cancers, including pancreatic cancer.

1. Introduction

Pancreatic cancer, one of the intractable solid tumors, is the fourth leading cause of cancer-related deaths in the United States and the fifth in Japan [1]. The average survival period of patients suffering from advanced pancreatic adenocarcinoma is still extremely short, only 6 months, despite recent progress in the chemotherapies [2]. Although cancer detection and treatment have been greatly improved through the development of diagnostic imaging modalities, it is still difficult to detect pancreatic cancer [3]. Consequently, the development of diagnostic systems to detect these cancers is of great importance.

Recently, superparamagnetic iron oxide (SPIO) nanoparticles composed of either magnetite (Fe_3O_4) or maghemite (g-Fe_2O_3) have been studied as contrast agents for magnetic resonance (MR) imaging [4]. Commercial application for human diagnosis based on SPIO particles is currently available. However, since cancer detection requires the systemic administration of iron oxide nanoparticles, the circulation time of the particles must be prolonged. Several studies have already reported that the behavior of magnetic nanoparticles in the bloodstream depends closely on their nanoscale morphology, including overall diameter, size distribution, or nature of the surface [5,6]. Additionally, the surface modification of iron oxide nanoparticles has proved a versatile strategy for improving their biological performance, including the reduction of immunogenicity and enhancement of targeted delivery to specific tissues [7]. However, the overall correlation between the surface modification of nanoparticles and their *in vivo* behavior remains to be further elucidated.

Various methods of stabilization for SPIO nanoparticles have been reported to date [8]. One of the most feasible approaches could be the stabilization of SPIO by coated with biocompatible polymers [9]. Suitable polymers, including poly(ethylene glycol) (PEG) and its block copolymers, are promising for the development of SPIO systems with defined surface properties. This coating of particles with PEG, or PEGylation, to avoid their uptake by the reticuloendothelial system, is under intensive investigation. We also previously reported the accumulation of β-FeOOH nanoparticles coated with PEG–poly(α,β-aspartic acid) block copolymer

* Corresponding author. Department of Materials Engineering, Graduate School of Engineering, The University of Tokyo, 7-3-1 Hongo, Bunkyo-ku, Tokyo 113-8656, Japan.
E-mail address: kataoka@bmw.t.u-tokyo.ac.jp (K. Kataoka).
[1] Equal contribution.

0168-3659/$ – see front matter © 2009 Elsevier B.V. All rights reserved.
doi:10.1016/j.jconrel.2009.06.002

(PEG–PAsp) into experimental colon adenocarcinoma, which could be applicable for tumor-selective MR imaging [10]. The multivalent bonding of PEG-based block copolymer to magnetic nanoparticles may thus help to facilitate the accumulation of these nanoparticles into some solid tumors. However, magnetic nanoparticles of any design have not yet been successful in exhibiting sufficient accumulation in intractable solid cancers, including pancreatic adenocarcinoma [1]. In addition to improving the performance of iron-based contrast agents (e.g. biocompatibility), the co-administration of adjuvant small molecules could increase the accumulation of these agents in target cancer tissue. In fact, we have recently shown that the administration of the small molecule TGF-β inhibitor (LY364947) at a low dose [11], which could minimize the potential side effects of the TGF-β inhibitor, can alter the tumor microenvironment and enhance the EPR effect in these cancers [12]. Therefore, the combined use of TGF-β inhibitor could be promising to diagnose intractable cancers with a long-circulating MRI contrast agent. Here, we demonstrated the successful MR imaging of experimental pancreatic cancer by the systemic administration of newly developed SPIO nanoparticles coated by PEG–PAsp in aid of TGF-β inhibitor.

2. Materials and methods

2.1. Reagents

β-benzyl L-aspartate and bis(trichloromethyl)carbonate (triphosgene) were purchased from Sigma-Aldrich Corporation (St. Louis, MO, USA) and Tokyo Chemical Industry Co., Ltd. (Tokyo, Japan), respectively. α-Methoxy-ω-amino-poly(ethylene glycol) (CH_3O–PEG–NH_2; $M_w = 12000$) was purchased from NOF Corporation (Tokyo, Japan). Tetrahydrofuran (THF), *n*-hexane, *N,N*-dimethylformamide (DMF), CH_2Cl_2 were doubly-distilled according to the standard procedures. The magnetite nanoparticles were supplied by Toda Kogyo Corporation (Hiroshima, Japan; average particle size of magnetite: 10 nm). Resovist® was obtained from Bayer HealthCare Co., Ltd. (Osaka, Japan). TGF-β inhibitor was purchased from EMD Chemicals Inc. (San Diego, CA, USA) (LY364947; catalog no. 616451).

2.2. Synthesis of poly(ethylene glycol)–poly(α,β-aspartic acid) block copolymer (PEG–PAsp)

PEG–PAsp was synthesized by a previously reported procedure [13]. Briefly, poly (ethylene glycol)–*b*–poly(β-benzyl L-aspartate) block copolymer (PEG–PBLA) was prepared by ring-opening polymerization of N-carboxy anhydride of β-benzyl L-aspartate (BLA-NCA) from the ω-NH_2 group of PEG ($M_w = 1.2 \times 10^4$). Molecular weight distribution of PEG–PBLA was narrow as $M_w/M_n = 1.06$, which was determined by gel permeation chromatography [columns: TSK-gel G3000HHR, G4000HHR (Tosoh, Yamaguchi, Japan); eluent: DMF containing 10 mM LiCl; flow rate: 0.8 ml/min; detector: refractive index (RI); temperature: 40 °C]. The composition of these block copolymers was determined by ^{1}H NMR from peak intensity ratios of methylene protons of PEG (OCH_2CH_2: $d = 3.7$ ppm) and phenyl protons of the β-benzyl groups of PBLA ($-CH_2C_6H_5$: $d = 7.3$ ppm). The polymerization degree of BLA in block copolymer was calculated to be 38. The benzyl groups of PEG–PBLA were then removed by alkaline hydrolysis using 0.1 N NaOH to obtain PEG–PAsp as follows:

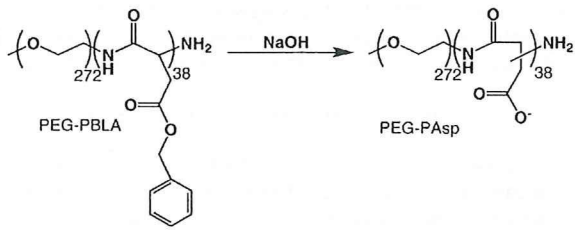

2.3. Preparation of PEG–PAsp-coated magnetite nanoparticles

PEG–PAsp-coated magnetite nanoparticles were prepared according to the previous method with slight modification [10]. Briefly, magnetite solution was quickly added to an aqueous solution of PEG–PAsp with varying feed molar ratios of aspartic acid residues to Fe ([Asp]/[Fe]) in the range of 0.01 to 1. The final concentration of magnetite was adjusted to 10 mmol/l. The mixed solutions were incubated at room temperature for 24 h to obtain magnetite nanoparticles coated with PEG–PAsp. Purification of the PEG–PAsp-coated magnetite nanoparticles was carried out by ultrafiltration (MWCO 200000; polysulfone membrane, Toyo Roshi Co. Ltd., Tokyo, Japan).

2.4. Physicochemical characterization of the nanoparticles

The morphology and size distribution of the nanoparticles were examined by transmission electron microscopy (H-7000, Hitachi, Ltd., Tokyo, Japan) at an accelerating voltage of 75 kV. The TEM samples were prepared by mounting a drop of aqueous iron oxide nanoparticles suspension on carbon-coated 400 mesh Cu grids and allowing them to dry in air. Fourier transform infrared (FT-IR) spectra were obtained using a FT-IR spectrophotometer (FT/IR615, JASCO Corporation, Hachioji, Tokyo, Japan) with a resolution of 4 cm^{-1}. To characterize the interaction between block copolymer and magnetite nanoparticles, a small amount of nanoparticles powder was milled with KBr, and then pressed into a disc for analysis. Each spectrum was scanned 64 times to increase the signal-to-noise ratio. The Fe content in the nanoparticles was determined by ion coupled plasma-mass spectroscopy (ICP-MS, 4500, Hewlett Packard, Palo Alto, CA, USA). The amount of adsorbed block copolymer on magnetite nanoparticles was measured by thermogravimetric analysis (TGA) (EXSTAR6200 TG/DTA, Seiko Instruments Inc., Chiba, Japan) in nitrogen atmosphere with a heating rate of 10 °C/min in the temperature range of 25–1100 °C.

2.5. Light scattering and ζ-potential measurements

The size distribution of the PEG–PAsp-coated magnetite nanoparticles was examined by dynamic light scattering (DLS) DLS-7000 (Otsuka Electronics Co., Ltd., Osaka, Japan). Vertically polarized light with a wavelength of 488 nm from an Ar-ion laser (15 mW) was used as the incident beam. All measurements were conducted at 37 °C, and the data were analyzed by the cumulant method to determine the hydrodynamic diameters of the particles. The ζ-potential of PEG–PAsp-coated magnetite nanoparticles at 37 °C was measured by a Zetasizer NanoZS instrument equipped with a DTS5001 cell (Malvern Instruments Ltd., Worcestershire, UK).

2.6. Characterization of the r_2 relaxivities

The MR contrast effect of the magnetite nanoparticles was examined by measuring their proton relaxivities, r_2, of which the definition is the slope of the concentration dependence given as:

$$1/T_2 = 1/T_2(0) + r_2[\mathrm{Fe}]$$

Thus, a plot of $1/T_2$ versus concentration gives the relaxivity as the slope, where T_2 is the transversal relaxation time, $1/T_2$ is the transversal relaxation rate constant in the presence of a paramagnetic species, and $1/T_2(0)$ is the transversal relaxation rate constant in the absence of a paramagnetic species. The magnetite nanoparticles were dispersed into deionized water at concentrations of 0.5, 1.0, 1.5, 2.0, and 2.5 mM and the T_2 of these nanoparticle solutions was measured at 25 °C in water with a 0.47 T minispectrometer (Minispec, Bruker

Optics Inc., Woodlands, TX, USA) using the Carr–Purcell–Meiboom–Gill (CPMG) method [14].

2.7. In vivo MR imaging

The BxPC3 human pancreatic adenocarcinoma cell line was obtained from the American Type Culture Collection (Manassas, VA, USA). The BxPC3 cells were grown in RPMI 1640 medium supplemented with 10% FBS. BALB/c nude mice (female, 5–6 weeks of age), obtained from Charles River Laboratories Japan Inc. (Tokyo, Japan), were inoculated subcutaneously with BxPC3 cells (1×10^7 cells/mouse). After 3–4 weeks, MR imaging of the tumors was conducted with a 4.7 T scanner (INOVA200, Varian, Inc., Palo Alto, CA, USA). Twenty-four hours prior to the *in vivo* MR imaging, animals were treated with TGF-β inhibitor, 5 mg/ml in 4 μl of DMSO and diluted by 100 μl of PBS, at 1 mg/kg by intraperitoneal injection. Subsequently, the mice were injected at a dose of 0.1 mmolFe/kg, with Resovist® or PEG–PAsp-coated magnetite nanoparticles. A total of 4 conditions ($n=5$ mice each) were investigated, i.e. with or without TGF-β inhibitor for both Resovist® or PEG–PAsp-coated magnetite nanoparticles. Imaging was performed at different temporal points (e.g., preinjection, 1 h postinjection, and 2 h postinjection). For the T_2-weighted MR imaging of live mice, the following parameters were adopted: spin-echo method, point resolution = 234×234 μm, section thickness = 2.0 mm, TE = 60 ms, TR = 3000 ms, number of acquisitions = 5. All animals were treated in accordance with the guidelines of the Animal Ethics Committee of the University of Tokyo.

2.8. Histology

The excised samples were fixed overnight in 4% paraformaldehyde and then paraffin-embedded. Embedded samples were thin sliced at 10 μm thick and then stained using an Iron Stain Kit (Muto Pure Chemicals Co., Ltd., Tokyo, Japan), based on McFadzean's protocol [15], with nuclear post-staining by 1% Safranin O. Iron staining was observed using an AX80 microscope (Olympus Corporation, Tokyo, Japan). The photographs were further quantified using Adobe Photoshop software (Adobe Systems Incorporated, San Jose, CA, USA), ImageJ software (National Institute of Health, MD, USA), and Microsoft Excel software (Microsoft Corporation, Redmond, WA, USA).

3. Results and discussion

3.1. The physicochemical properties of the PEG–PAsp-coated magnetite nanoparticle: diameter and surface polymer density

For solid tumor diagnosis, it is important to develop well-designed magnetite nanoparticles. The key physicochemical properties of magnetite nanoparticles are size, surface polymer density, and surface charge, since these characteristics can affect accumulation of magnetite nanoparticles to solid tumor. The PEG–PAsp-coated magnetite nanoparticles were prepared by mixing solutions of magnetite nanoparticles and PEG–PAsp with various molar ratios of the Asp residues to Fe (Asp/Fe); Asp/Fe ranged from 0.01 to 0.5, where [Fe] = 10 mmol/l. As seen in Fig. 1, the transmission electron microscopy (TEM) image with 75 kV accelerating voltage of nanoparticles mounted on carbon grid from aqueous solution revealed that PEG–PAsp-coated magnetite nanoparticles take a cubic shape with a mean particle diameter of approximately 10 nm. The PEG–PAsp coating was observed as a layer with a thickness of approximately 5 nm, surrounding the magnetite nanoparticles. It was also observed in the TEM image that these PEG–PAsp-coated nanoparticles form clusters with a size range of 100 nm.

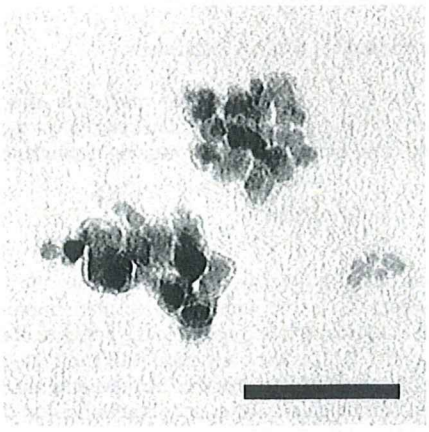

Fig. 1. TEM image of the PEG–PAsp-coated magnetite nanoparticles. Bar: 100 nm.

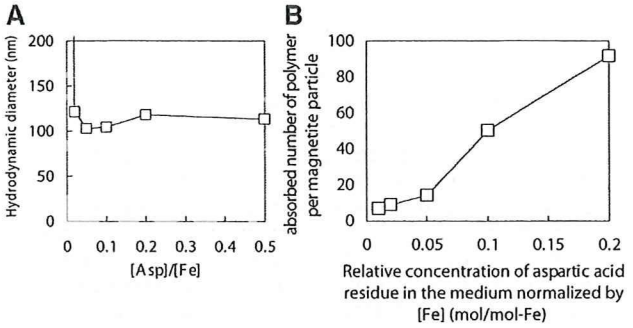

Fig. 2. Physicochemical properties of the PEG–PAsp-coated magnetite nanoparticles. (A) Hydrodynamic diameter vs. relative concentration of aspartic acid residue in the medium normalized by [Fe] (mol/mol-Fe) (=[Asp]/[Fe]), and (B) Change in the adsorbed density of PEG–PAsp on the magnetite surface estimated from TGA analysis with a bulk concentration of PEG–PAsp. Temperature = 37 °C; medium: distilled water.

The hydrodynamic diameter of these nanoparticles in aqueous medium was then measured with DLS and shown to be in the range of 100 to 120 nm with unimodal distribution, for Asp/Fe ratios ranging from 0.02–0.5. This DLS data is consistent with the cluster formation of nanoparticles indicated from TEM images. However, with a lowered Asp/Fe ratio as 0.01, the hydrodynamic diameter increased significantly (Fig. 2A). This result indicates that there is a critical surface concentration of PEG to effectively prevent the PEG–PAsp-coated magnetite nanoparticles from the agglomeration. The purified nanoparticles were stable in distilled water as 100 nm-scaled cluster at room temperature as well as at 37 °C, maintaining the initial photon count and distribution in DLS analysis for at least one month, even after the ultrafiltration to remove free PEG–PAsp possibly remained in the reactant.

The density of the PEG–PAsp block copolymer on the magnetite particle surface was estimated by TGA. Here, nanoparticles were heated in the nitrogen atmosphere to selectively vaporize the polymer fraction. Eventually, the amount of absorbed polymer on the surface of the nanoparticles was measured from the weight change by heating. The polymer density was then calculated from the TGA measurement for all the nanoparticles, assuming the cubic morphology as evidenced by microscopy and a density of 5.05 g/cm^3 for magnetite. As seen in Fig. 2B, the number of polymer strands on the nanoparticle surface was as high as 100. This data suggests that the PEG density on the magnetite nanoparticles is a little lower than that of PEGylated gold nanoparticles prepared through the surface tethering of PEG-SH [16].

3.2. The mechanism of PEG–PAsp adsorption on the magnetite nanoparticles

To confirm the formation of PEG–PAsp coating on the magnetite nanoparticles, the ζ-potential of bare and PEG–PAsp-coated magnetite nanoparticles was measured in 10 mM MOPS buffer as a function of

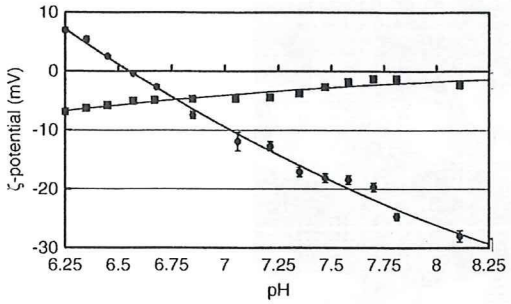

Fig. 3. Change in the ζ-potential with pH for bare (●) and PEG–PAsp-coated (■) magnetite nanoparticles. Temperature = 37 °C; medium: 10 mM MOPS buffer.

pH (Fig. 3). The isoelectric point (IEP) of the bare magnetite nanoparticles was estimated as approximately 6.6, which is consistent with the reported IEP value of iron oxide [17]. In a lower pH (below the IEP), the magnetite nanoparticle surface was protonated to result in a positive ζ-potential. Thus, in this pH range, electrostatic attraction between positively-charged magnetite nanoparticles and negatively charged PEG–PAsp is expected to occur, allowing the PEG–PAsp adsorption to the nanoparticle surface. Alternatively, the bare magnetite nanoparticles possess negative ζ-potential at physiological pH 7.4, whereas the ζ-potential shifted to the neutral value for PEG–PAsp modified nanoparticles in 10 mM MOPS buffer (pH 7.4), being consistent with the formation of a PEG shell layer. Also, these data suggest that there should be an adsorption mechanism other than simple electrostatic interaction, because magnetite has a negative ζ-potential value at pH 7.4 to induce electrostatic repulsive force against negatively charged carboxylates in PEG–PAsp. The adsorption mechanism under physiological pH was suggested to be the monodentate chelation (I) (Fig. 4) from the result of Fourier transform infrared spectroscopy [18], as explained in detail in Supplemental Text with Supplemental Fig. 1 and Supplemental Table 1.

3.3. Comparison study of the physicochemical characteristics of the PEG–PAsp- and dextran-coated magnetite nanoparticles

The MRI detection limit was compared between the PEG–PAsp- and dextran-coated magnetite nanoparticles in the field of 0.47 T at 25 °C from the relaxivity r_2, exhibiting the sensitivity of the T_2 MRI contrast agent. The dextran-coated magnetite used in this study was the one already in clinical use, Resovist®. Eventually, the relaxivity r_2 of the PEG–PAsp nanoparticle was calculated to be 138 $mM^{-1}s^{-1}$, the value similar to Resovist® [19].

The hydrodynamic diameter observed between the PEG–PAsp-coated and dextran-coated magnetite nanoparticles differed significantly in an NaCl-concentration-dependent manner (Fig. 5A). Although the hydrodynamic diameter of the PEG–PAsp-coated magnetite nanoparticles did not change significantly up to 3 M NaCl, indicating the appreciable stability of the PEG–PAsp-coating, that of Resovist® significantly increased even at NaCl = 0.15 M, and reached more than 1 μm at NaCl = 0.5 M, due to the drastic aggregation. Note that the PEG–PAsp-coated nanoparticles did not show any change in

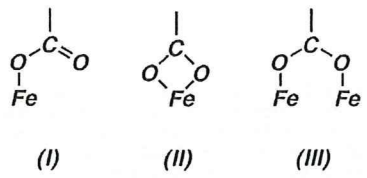

Fig. 4. Modes of carboxylate-metal complexation: monodentate (**I**), bidentate chelating (**II**), and bidentate bridging (**III**).

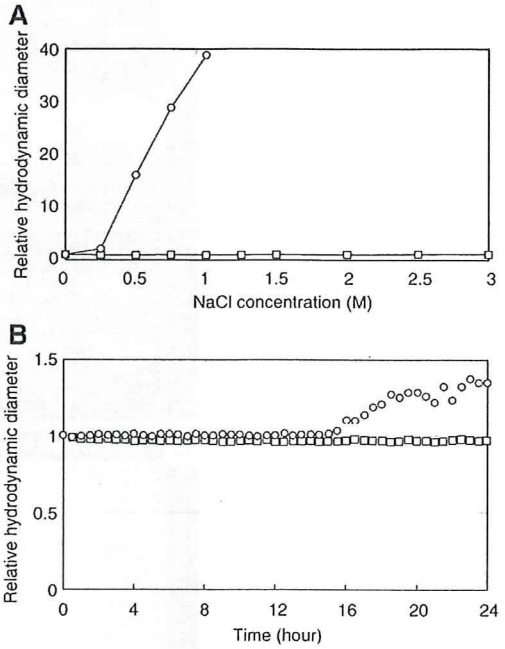

Fig. 5. NaCl concentration (A) and time (B) dependencies of the relative hydrodynamic diameter of magnetite nanoparticles, □: PEG–PAsp-coated nanoparticles, ○: dextran-coated nanoparticles (Resovist®). Fe concentration = 2 mmol/l; temperature = 37 °C; medium 10 mM Tris–HCl buffered saline (pH 7.4). 10% fetal bovine serum was contained in (B).

their size even after one month storage in 10 mM Tris–HCl buffered saline (pH 7.4, 37 °C) (data not shown).

The colloidal stability of the PEG–PAsp-coated magnetite nanoparticles in physiological conditions was also examined. We incubated them in 10 mM Tris–HCl buffered saline (pH 7.4) containing 10% fetal bovine serum at 37 °C for 24 h and measured the change of the hydrodynamic diameter (Fig. 5B). The size of the PEG–PAsp-coated magnetite nanoparticles did not obviously change during the 24-hour storage time. On the other hand, the size of Resovist® increased by the formation of aggregates after 16 h of storage time.

The stability of the PEG–PAsp-coated nanoparticles may come from the multivalent bonding between flanking carboxylic groups and the magnetite surface, as suggested by FT-IR study. These findings are consistent with a report showing that PEG-oligo(aspartic acid) block copolymer-coated iron oxide nanoparticles were stable at pH 2–11 and in 1 M NaCl, where the repeating number of aspartic acid units was 3 or more [20]. In contrast, instability of Resovist® against salt addition may be due to weak interaction between magnetite and hydroxyl groups of dextran [21].

3.4. MR imaging of experimental pancreatic cancer in vivo

The MR imaging of tumor tissue *in vivo* was then conducted by comparing PEG–PAsp- and dextran-coated magnetite nanoparticles, Resovist®. Resovist® has already been approved for clinical use as a liver-specific MRI contrast agent, due to accumulation into the reticuloendothelial system (RES) of the normal liver. Most malignant liver tumors do not contain RES cells and therefore are contrasted positive by Resovist®. A xenografted BxPC3 human pancreatic adenocarcinoma cell line in nude mice, characterized histologically by fibrosis and hypovascularity, was used as a model of intractable cancer. Recently, we reported that the administration of TGF-β inhibitor to tumor model mice significantly enhanced the intratumoral accumulation of nanoparticles encapsulating anticancer drugs [11]. Thus, we tested the effect of the i.p. administration of TGF-β

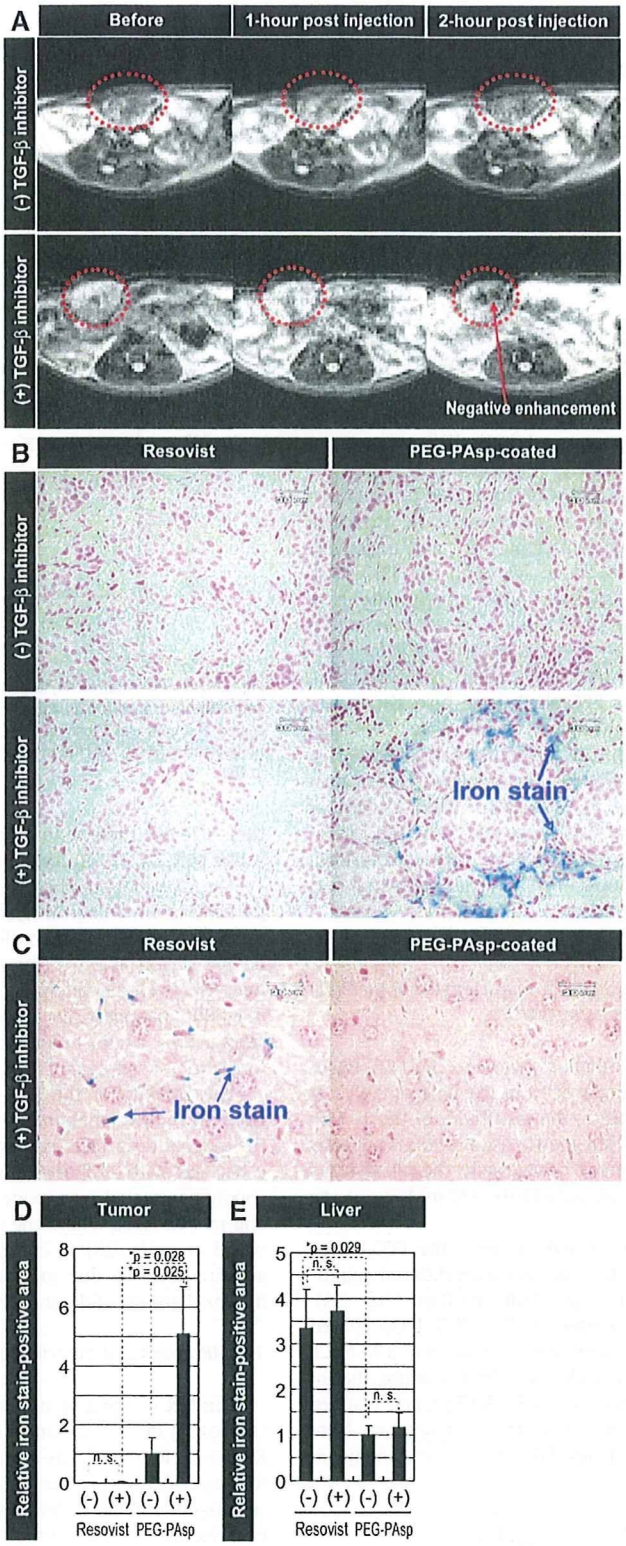

Fig. 6. MR imaging of experimental pancreatic cancer *in vivo* and the distribution of the nanoparticles in cancer and liver tissues. (A) T_2-weighted images of tumor-implanted mice (tumor sites are circled by red dotted line) at different temporal points after injection of PEG–PAsp-coated magnetite nanoparticles and TGF-β inhibitor. All images were obtained in a field strength of 4.7 T. (B) Histological sections of BxPC3 xenograft stained with Prussian blue. The distribution of Resovist® and PEG–PAsp-coated magnetite nanoparticles, at 5.5 mg/kg with and without TGF-β inhibitor at 1 mg/kg, were examined 24 h after the administration. (C) Histological sections of liver stained with Prussian blue. The distribution of Resovist® and PEG–PAsp-coated magnetite nanoparticles, at 5.5 mg/kg with TGF-β inhibitor at 1 mg/kg, was examined 24 h after the administration. (D and E) Areas of iron staining in the tumor and liver were quantified. PEG–PAsp, PEG–PAsp coated magnetite nanoparticles with (+) and without (−) inhibitor. Error bars in the graphs represent standard errors of the mean ($n = 6$), and P values were calculated by two-tailed Student's t test. n.s.: not significant.

inhibitor with the i.v. administration of Resovist® or the PEG–PAsp-coated magnetite nanoparticles on their imaging capability in size-matched xenografts of the BxPC3 cell line. Fig. 6A shows the T_2-weighted MR images of the tumors at different time periods after the intravenous administration (preinjection, and 1 and 2 h postinjection) of PEG–PAsp-coated magnetite nanoparticles with and without TGF-β inhibitor.

Resovist® failed to image the tumor even with the co-administration of TGF-β inhibitor, presumably due to the non-specific accumulation into the reticuloendothelial system [8]. In contrast, the PEG–PAsp-coated magnetite nanoparticles exhibited significant negative enhancement of signal intensity in the tumor region of T_2-weighted images when combined with TGF-β inhibitor, suggesting the accumulation of detectable amounts of the PEG–PAsp-coated magnetite nanoparticles within 2 h after injection. Therefore, the difference in behavior of these two types of magnetite nanoparticles *in vivo* had a crucial importance in achieving effective tumor accumulation for successful MR imaging.

To further verify the accumulation of iron oxide nanoparticles in the tumor, we performed Prussian blue staining of the tumor tissues to detect iron oxide, which stains blue. As shown in Fig. 6B, positive staining of the tumor for iron oxide was only obvious in the condition with PEG–PAsp-coated nanoparticles combined with the TGF-β inhibitor. Areas of iron staining in the tumor were then quantified as seen in Fig. 6D, demonstrating a significant increase in the areas of positive staining by TGF-β inhibitor treatment. The presence of iron oxide was consistent with the MRI results. Iron oxide was observed in the area rich in fibrotic components, suggesting that the administration of TGF-β inhibitor transiently increases the permeability of the tumor capillary to promote the extravasation of the PEG–PAsp-coated magnetite nanoparticles, even though the BxPC3 tumor has the characteristic of hypovascularity [11].

Lastly, we examined liver tissues from the mice treated with Resovist® or the PEG–PAsp-coated magnetite nanoparticle, with or without TGF-β inhibitor, by iron staining (Fig. 6C). Although aggregates of Resovist® accumulated in the liver, particularly in cells with smaller nuclei (presumably Kuppfer cells), far less PEG–PAsp-coated magnetite nanoparticles accumulated in the liver without aggregation. These results did not differ with or without TGF-β inhibitor, which was determined by the area of Prussian blue staining (Fig. 6E).

4. Conclusion

In conclusion, we here demonstrated the physicochemical properties of PEG–PAsp-coated magnetite nanoparticles and the feasibility of these nanoparticles as MR contrast agents for cancer diagnosis. Improving the stability of nanoparticles might be important for enabling a longer half-life in the bloodstream and a better accumulation in tumor tissue, leading to effective MR imaging with contrast agents. The neutral ζ-potential of the PEG–PAsp-coated nanoparticle may contribute to avoidance of reticuloendothelial system uptake. Formation of the stable and dense PEG layer on the magnetite surface through the anchoring of PEG–PAsp by the monodentate chelation of COO^- residues to iron atoms definitely plays a substantial role in the increased stability of the nanoparticles *in vivo*. The use of PEG–PAsp-coated magnetite nanoparticles combined with a TGF-β inhibitor could thus become a novel regime in the diagnosis of intractable cancers, including pancreatic adenocarcinoma.

Acknowledgements

The authors thank Dr James R. Christie II, The University of Tokyo, for editing the English of the manuscript. This work was supported by a Grant-in-Aid for Scientific Research from the Ministry of Education, Culture, Sports, Science and Technology (MEXT), Core Research for Evolution of Science and Technology (CREST), Japan Science and Technology Corporation (JST), and the 21st century COE program 'Human-Friendly Materials based on Chemistry' from MEXT.

Appendix A. Supplementary data

Supplementary data associated with this article can be found, in the online version, at doi:10.1016/j.jconrel.2009.06.002.

References

[1] M.R. Dreher, W. Liu, C.R. Michelich, M.W. Dewhirst, F. Yuan, A. Chilkoti, Tumor vascular permeability, accumulation, and penetration of macromolecular drug carriers, J. Natl. Cancer Inst. 98 (5) (2006) 335–344.
[2] H.A. Burris, M.J. Moore, J. Andersen, M.R. Green, M.L. Rothenberg, M.R. Modiano, M.C. Cripps, R.K. Portenoy, A.M. Storniolo, P. Tarassoff, R. Nelson, F.A. Dorr, C.D. Stephens, D.D. Von Hoff, Improvements in survival and clinical benefit with gemcitabine as first-line therapy for patients with advanced pancreas cancer: a randomized trial, J. Clin. Oncol. 15 (6) (1997) 2403–2413.
[3] D.V. Sahani, Z.K. Shah, O.A. Catalano, G.W. Boland, W.R. Brugge, Radiology of pancreatic adenocarcinoma: current status of imaging, J. Gastroenterol. Hepatol. 23 (1) (2008) 23–33.
[4] D.L. Huber, Synthesis, properties, and applications of iron nanoparticles, Small 1 (5) (2005) 482–501.
[5] R. Weissleder, G. Elidonzo, J. Wittenberg, C.A. Rabito, H.H. Bengele, L. Josephson, Ultrasmall superparamagnetic iron oxide: characterization of a new class of contrast agents for MR imaging, Radiology 175 (2) (1990) 489–493.
[6] M. Lewin, N. Carlesso, C.H. Tung, X.W. Tang, D. Cory, D.T. Scadden, R. Weissleder, Tat peptide-derivatized magnetic nanoparticles allow *in vivo* tracking and recovery of progenitor cells, Nat. Biotechnol. 18 (4) (2000) 410–414.
[7] Y.W. Jun, J.H. Lee, J. Cheon, Chemical design of nanoparticle probes for high-performance magnetic resonance imaging, Angew. Chem. Int. Ed. 47 (28) (2008) 5122–5135.
[8] D.D. Stark, R. Weissleder, G. Elizondo, et al., Superparamagnetic iron oxide: clinical application as a contrast agent for MR imaging of the liver, Radiology 168 (2) (1988) 297–301.
[9] T. Neuberger, B. Schöpf, H. Hofmann, M. Hofmann, B. von Rechenberg, Superparamagnetic nanoparticles for biomedical applications: possibilities and limitations of a new drug delivery system, J. Magn. Mater. 293 (1) (2005) 483–496.
[10] M. Kumagai, Y. Imai, T. Nakamura, Y. Yamasaki, M. Sekino, S. Ueno, K. Hanaoka, K. Kikuchi, T. Nagano, E. Kaneko, K. Shimokado, K. Kataoka, Iron hydroxide nanoparticles coated with poly(ethylene glycol)–poly(aspartic acid) block copolymer as novel magnetic resonance contrast agents for *in vivo* cancer imaging, Colloids Surf. B: Biointerfaces 56 (1–2) (2007) 174–181.
[11] M.R. Kano, Y. Bae, C. Iwata, Y. Morishita, M. Yashiro, M. Oka, T. Fujii, A. Komuro, K. Kiyono, M. Kaminishi, K. Hirakawa, Y. Ouchi, N. Nishiyama, K. Kataoka, K. Miyazono, Improvement of cancer-targeting therapy, using nanocarriers for intractable solid tumors by inhibition of TGF-β signaling, Proc. Natl. Acad. Sci. U. S. A. 104 (9) (2007) 3460–3465.
[12] Y. Matsumura, H. Maeda, A new concept for macromolecular therapeutics in cancer-chemotherapy-mechanism of tumoritropic accumulation of proteins and the antitumor agent SMANCS, Cancer Res. 46 (12) (1986) 6387–6392.
[13] N. Nishiyama, M. Yokoyama, T. Aoyagi, T. Okano, Y. Sakurai, K. Kataoka, Preparation and characterization of self-assembled polymer-metal complex micelle from cis-dichlorodiammineplatinum(II) and poly(ethylene glycol)–poly(alpha,beta-aspartic acid) block copolymer in an aqueous medium, Langmuir 15 (2) (1999) 377–383.
[14] E. Fukushima, S.B.W. Roeder (Eds.), Experimental pulse NMR: a nuts and bolts approach, Addison-Wesley, Reading, Mass, 1981, pp. 28–35.
[15] A.J.S. MacFadzean, L.J. Davis, Iron-staining erythrocytic inclusions with especial reference to acquired haemolytic anaemia, Glasgow Med. J. 28 (1947) 237–279.
[16] S. Takae, Y. Akiyama, H. Otsuka, T. Nakamura, Y. Nagasaki, K. Kataoka, Ligand density effect on biorecognition by PEGylated gold nanoparticles: regulated interaction of RCA120 lectin with lactose installed to the distal end of tethered PEG strands on gold surface, Biomacromolecules 6 (2) (2005) 818–824.
[17] L. Cromières, V. Moulin, B. Fourest, E. Giffaut, Physico-chemical characterization of the colloidal hematite/water interface: experimentation and modeling, Colloids Surf., A. Physicochem. Eng. Asp. 202 (1) (2002) 101–115.
[18] L.J. Kirwan, P.D. Fawell, W. van Bronswijk, In situ FTIR-ATR examination of poly (acrylic acid) adsorbed onto hematite at low pH, Langmuir 19 (14) (2003) 5802–5807.
[19] Y.X.J. Wang, S.M. Hussain, G.P. Krestin, Superparamagnetic iron oxide contrast agents: physicochemical characteristics and applications in MR imaging, Eur. Radiol. 11 (11) (2001) 2319–2331.
[20] S.R. Wan, J.S. Huang, M. Guo, H. Zhang, Y. Cao, H. Yan, K. Liuet, Biocompatible superparamagnetic iron oxide nanoparticle dispersions stabilized with poly (ethylene glycol)oligo(aspartic acid) hybrids, J. Biomed. Mater. Res. A 80A (4) (2007) 946–954.
[21] C.W. Jung, Surface-properties of superparamagnetic iron-oxide MR contrast agents — ferumoxides, ferumoxtran, ferumoxsil, Magn. Reson. Imaging 13 (5) (1995) 675–691.

Enhanced Percolation and Gene Expression in Tumor Hypoxia by PEGylated Polyplex Micelles

Muri Han[1], Makoto Oba[2], Nobuhiro Nishiyama[3,4], Mitsunobu R Kano[4,5], Shinae Kizaka-Kondoh[6] and Kazunori Kataoka[1,3,4,7]

[1]Department of Materials Engineering, Graduate School of Engineering, The University of Tokyo, Tokyo, Japan; [2]Department of Clinical Vascular Regeneration, Graduate School of Medicine, The University of Tokyo, Tokyo, Japan; [3]Center for Disease Biology and Integrative Medicine, Graduate School of Medicine, The University of Tokyo, Tokyo, Japan; [4]Center for NanoBio Integration, The University of Tokyo, Tokyo, Japan; [5]Department of Molecular Pathology, Graduate School of Medicine, The University of Tokyo, Tokyo, Japan; [6]Department of Radiation Oncology and Image-Applied Therapy, Kyoto University, Graduate School of Medicine, Kyoto, Japan; [7]Core Research for Evolutional Science and Technology (CREST), Japan Science and Technology Agency (JST), Kawaguchi, Japan

In regard to gene vectors for cancer gene therapy, their percolation into the tumor tissue should be essential for successful outcome. Here, we studied the tumor penetrability of nonviral vectors (polyplexes) after incubation with the multicellular tumor spheroid (MCTS) models and intratumoral (i.t.) injection into subcutaneous tumors. As a result, polyethylene glycolated (PEGylated), core–shell type polyplexes (polyplex micelles) showed facilitated percolation and improved transfection inside the tumor tissue, whereas conventional polyplexes from cationic polymers exhibited limited percolation and localized transfection. Furthermore, the transfection of hypoxia-responsive plasmid demonstrated that polyplex micelles allowed the transfection to the hypoxic region of the tumor tissue in both *in vitro* and *in vivo* experiments. To the best of our knowledge, our results demonstrated for the first time that polyplex micelles might show improved tumor penetrability over cationic polyplexes, thereby achieving transfection into the inside of the tumor tissue.

Received 22 December 2008; accepted 24 April 2009; published online 26 May 2009. doi:10.1038/mt.2009.119

INTRODUCTION

Gene therapy is a promising method for the treatment of malignant tumors, and its success relies on the capabilities of gene vectors. In this regard, nonviral vectors composed of plasmid DNA (pDNA) and cationic polymers, so-called polyplexes have been attracting much attention due to several advantages such as no immunogenicity, safety, and easy large-scale preparation.[1–4] So far, considerable efforts have been devoted to improve the transfection efficiency of polyplexes as well as control the gene expression in the body.[5–8] However, in regard to gene vectors for cancer gene therapy, much attention should be paid on another important property: percolation into the tumor tissue. In general, solid tumors are known to possess heterogeneous structures composed of blood vessels, interstitial tissues, clusters of tumor cells with normoxic and hypoxic regions. Therefore, it might be difficult to deliver the therapeutic agents to tumor cells distant from the vasculature.[9–11] Furthermore, hypoxic region induced by the insufficient blood supply is known to be inherently less susceptible to therapeutic agents.[10] As such difficulty in treating hypoxic regions is often correlated with recurrence and malignant progression of solid tumors,[10] overcoming the limited drug access to hypoxic cells should be a critical issue in cancer therapy. Thus, the percolation of gene vectors in solid tumors should be of primary importance to achieve successful cancer gene therapy.

Recently, we have developed a highly transfectable but less-toxic core–shell type polyplex with poly(ethylene glycol) (PEG) palisades (polyplex micelle), which was formed through the electrostatic interaction between pDNA and PEG-*b*-polyaspartamide having 1,2-diaminoethane side chain (PEG-*b*-P[Asp(DET)]) (**Figure 1**).[12,13] This polyplex micelle showed remarkable features, including efficient gene transfer to primary cells,[12] successful *in vivo* transfection to a rabbit carotid artery,[14] and transfection-mediated bone regeneration.[15] In this study, we explored the tumor penetrability of polyplex micelles, because we have recently demonstrated that amphiphilic block copolymer micelles can show penetrability into multicellular tumor spheroids (MCTSs)[16] as well as solid tumors after intravenous administration.[17] Here, we demonstrated that polyplex micelles from PEG-*b*-P[Asp(DET)] showed successful transfection to hypoxic cells inside MCTS as well as enhanced percolation and widely distributed gene expression within the tumor tissue after intratumoral (i.t.) injection. In contrast, cationic polyplexes showed limited penetration and localized transfection in both *in vitro* and *in vivo* studies. These results suggest that polyplex micelles may overcome the transport barrier of nonviral vectors, facilitating their use for cancer gene therapy.

RESULTS

Transfection to MCTS

MCTS is an appropriate *in vitro* tumor model representing morphological and functional features of *in vivo* avascular solid tumors, and is composed of actively proliferating outer cell layers

Correspondence: Kazunori Kataoka, Department of Materials Engineering, Graduate School of Engineering, The University of Tokyo, 7-3-1 Hongo, Bunkyo-ku, Tokyo 113-8656, Japan. E-mail: kataoka@bmw.t.u-tokyo.ac.jp

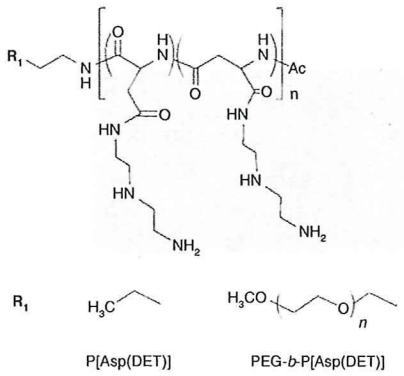

Figure 1 Chemical structures of P[Asp(DET)] homopolymers and PEG-*b*-P[Asp(DET)] block copolymers.

and hypoxic and quiescent inner cells.[18] In this study, a large-sized MCTS (400–500 μm), which possessed a hypoxic region characterized by necrotic cells inside due to limited supply of oxygen and nutrition (**Figure 2a**), was transfected with pCAcc + *Venus* by using the linear polyethylenimine (LPEI) and P[Asp(DET)] polyplexes and PEG-*b*-P[Asp(DET)] polyplex micelles at a defined mixing ratio of the number of amino groups units to a nucleotide unit (N/P ratio). Note that, although we have recently reported that a small-sized MCTS (~100 μm) can be disrupted by the cytotoxicity of polyplexes,[19] the large-sized MCTS used in this study is stable against the polyplex-mediated transfection. The expression of a variant of yellow fluorescent protein, *Venus* was evaluated by confocal microscopic observation. At 48 hours after the transfection (24-hour incubation and additional 24-hour incubation after the medium replacement), the LPEI polyplexes (N/P = 6, the manufacturer's recommendation ratio) and P[Asp(DET)] polyplexes (N/P = 20) showed significant gene expression limited to the periphery of the MCTS (**Figure 2b**). This result indicates that cationic polyplexes might lack the ability to transfect the inside of the MCTS. In contrast, PEG-*b*-P[Asp(DET)] polyplex micelles (N/P = 20) showed appreciable gene expression at not only the periphery but also the inside of the MCTS (**Figure 2b**), where a great number of necrotic cells were observed as indicated by red fluorescence from ethidium homodimer (EthD-1) (**Figure 2c**). These results suggest that polyplex micelles may allow the gene transfer to tumor cells in the hypoxic inner region of the MCTS.

Hypoxia-selective gene expression in the MCTS

To confirm the gene expression in hypoxic cells in the MCTS, we carried out the transfection study using pDNA encoding *Venus* driven by the 5× hypoxia-responsive element (5HRE) promoter (p5HRE + *Venus*). The hypoxia-selectivity of p5HRE + *Venus* was examined in monolayer cultured HuH-7 cells under hypoxic conditions reproduced by iron-chelating agent, deferoxamine mesylate.[20] As shown in **Figure 3a**, PEG-*b*-P[Asp(DET)] polyplex micelles containing hypoxia-responsive p5HRE + *Venus* showed no gene expression under normoxic conditions (0 μmol/l deferoxamine mesylate) but an appreciable gene expression under hypoxia-mimicking conditions (200 μmol/l deferoxamine mesylate). Note that polyplex micelles containing hypoxia-irresponsive pCAcc + *Venus* exhibited significant

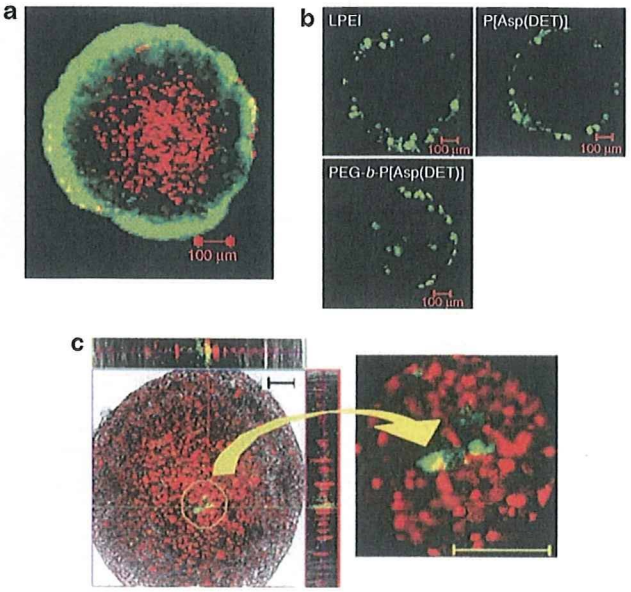

Figure 2 Transfection to HuH-7 MCTS. (**a**) Live/dead staining of HuH-7 spheroid (optical slice at the middle of spheroid. Bar = 100 μm). The green and red fluorescence are derived from live and dead cells, respectively. (**b**) Gene expression of pCAcc + *Venus* in HuH-7 MCTS transfected with LPEI polyplexes (N/P = 6), P[Asp(DET)] polyplexes (N/P = 20), and PEG-*b*-P[Asp(DET)] polyplex micelles (N/P = 20) (24 hours of incubation time and 24 hours of additional incubation after the medium replacement). (**c**) Gene expression of pCAcc + *Venus* at the inner region of HuH-7 MCTS transfected with PEG-*b*-P[Asp(DET)] polyplex micelles (N/P = 20) (24 hours of incubation time and 24 hours of additional incubation after the medium replacement) (Left: The red and green fluorescence are derived from dead cells and transfected protein *Venus*, respectively. Right: Magnified image of the circled region in the left picture). LPEI, linear polyethylenimine; MCTS, multicellular tumor spheroid; N/P, ratio of the number of amino groups units to a nucleotide unit.

gene expression under both normoxic and hypoxic conditions. Thus, p5HRE + *Venus* was demonstrated to be highly selective to hypoxic environments. Then, LPEI and P[Asp(DET)] polyplexes and PEG-*b*-P[Asp(DET)] polyplex micelles containing p5HRE + *Venus* were applied to the transfection to the large-sized MCTS (400–500 μm). As a result, none of 5 spheroids transfected with LPEI polyplexes showed the expression of p5HRE + *Venus* (data not shown), which may be consistent with the expression of pCAcc + *Venus* limited to the periphery of the MCTS (**Figure 2b**). Surprisingly, P[Asp(DET)] polyplexes exhibited the expression of p5HRE + *Venus* in two of five spheroids at 48 hours after the transfection; however, the gene expression was limited to the outer rims of hypoxic regions at ~100 μm distance from the periphery of the MCTS (**Figure 3b**; the yellow circle is the initial size of spheroids before the transfection). This result suggests that P[Asp(DET)] polyplexes could penetrate into the inside of the spheroids to some extent. In contrast, PEG-*b*-P[Asp(DET)] polyplex micelles allowed the transfection of p5HRE + *Venus* to a larger number of the cells in the inner region of the MCTS in 7 of 10 spheroids (**Figure 3b**), suggesting the ability of the polyplex micelles to transfect hypoxic cells inside of the spheroids. To further confirm this effect, two distinct plasmids encoding DsRedC1 (red fluorescence) driven

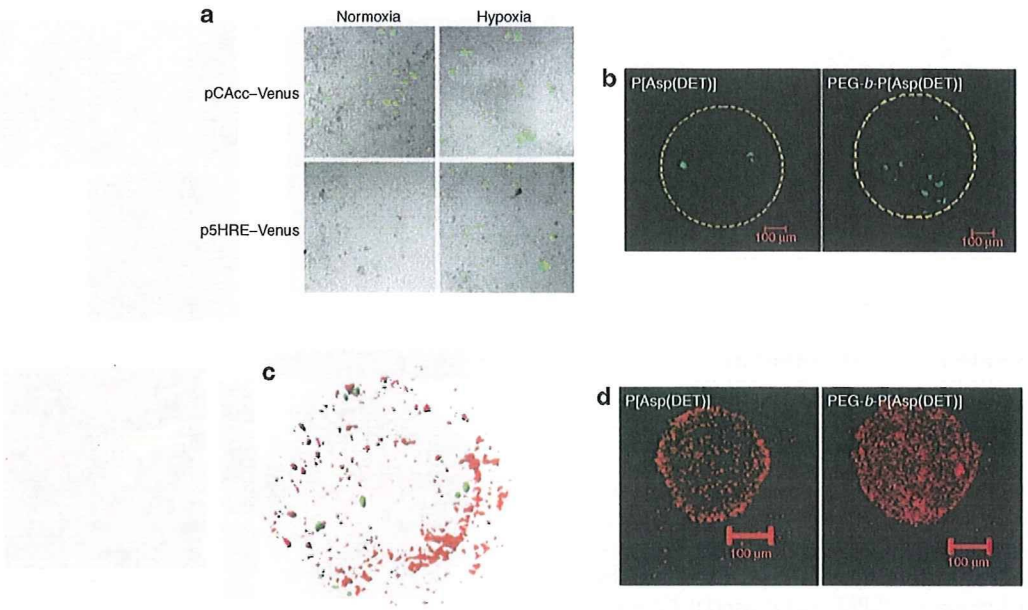

Figure 3 Hypoxia selective gene expression in the MCTS. (**a**) Gene expressions of hypoxia-irresponsive pCAcc + *Venus* and hypoxia-responsive p5HRE + *Venus* in monolayer cultured HuH-7 cells under normoxic and hypoxic conditions. HuH-7 cells were incubated with PEG-*b*-P[Asp(DET)] polyplex micelles (N/P = 20) for 24 hours, followed by additional 24 hours incubation after the medium replacement. Hypoxia-mimicking conditions were reproduced by incubating the cells with iron chelating agent, DFx during the postincubation. (**b**) Gene expressions of hypoxia-responsive p5HRE + *Venus* in the HuH-7 spheroids transfected with P[Asp(DET)] polyplexes and PEG-*b*-P[Asp(DET)] polyplex micelles (N/P = 20). The yellow circle indicates the size of the MCTS at the time of the transfection. (**c**) Piled up images of the gene expressions of hypoxia-irresponsive pCMV-DsRedC1 (red fluorescence) and hypoxia-responsive p5HRE – *Venus* (green fluorescence) in the MCTS transfected with PEG-*b*-P[Asp(DET)] polyplex micelles incorporating each plasmid (N/P = 20). (**d**) Distribution of Cy3-labeled pDNA encapsulated into P[Asp(DET)] polyplexes (N/P = 20) and PEG-*b*-P[Asp(DET)] polyplex micelles (N/P = 20) in HuH-7 MCTS after 24-hour incubation. The images were taken at the center of the spheroids. DFx, deferoxamine mesylate; MCTS, multicellular tumor spheroid; N/P, ratio of the number of amino groups units to a nucleotide unit.

by the cytomegalovirus (CMV) promoter (pCMV-DsRedC1) and *Venus* (green fluorescence) driven by the 5HRE promoter (p5HRE – *Venus*) were independently encapsulated into PEG-*b*-P[Asp(DET)] polyplex micelles, and then applied to the transfection to the MCTS. After 48 hours, optical slices of the MCTS at a depth of 1 μm were taken by confocal microscopy, and then piled up by Imaris software (Carl Zeiss, Jena, Germany) to obtain the three-dimensional localization of each fluorescence. As shown in Figure 3c, the expression of p5HRE – *Venus* was mainly detected in the inner region of the MCTS, whereas the expression of pCMV-DsRedC1 was observed throughout the MCTS. Thus, the hypoxic inner regions of the MCTS were successfully transfected with PEG-*b*-P[Asp(DET)] polyplex micelles.

Percolation of polyplexes and polyplex micelles into the MCTS

The percolation of the polyplexes and polyplex micelles into the MCTS was investigated by using Cy3-labeled pDNA. In this study, the MCTS with a diameter of 200–250 μm was used to detect weak fluorescence from Cy3-labeled pDNA within the spheroids. Figure 3d shows the fluorescent image of Cy3-labeled pDNA at the center of HuH-7 MCTS after 24-hour incubation with polyplexes or polyplex micelles. Note that the treatment of the relatively small-sized MCTS with LPEI polyplexes resulted in destruction of spheroid structures due to the cytotoxicity of LPEI as previously reported.[19] As shown in Figure 3d, P[Asp(DET)] polyplexes displayed apparent fluorescence at the periphery of spheroids. This result is consistent with the previous report that cationic polyplexes could penetrate only the outer 3–5 proliferating cell layers (10–20 μm) of the MCTS.[11] In contrast, the pDNA formulated in PEG-*b*-P[Asp(DET)] polyplex micelles showed well-distributed fluorescence within spheroids, suggesting their percolation into the inside of the spheroids. Similar results were obtained when the MCTS model from a different cell line (*i.e.*, human pancreatic BxPC3 cells) were used (**Supplementary Figure S1**). Thus, polyplex micelles might possess the ability to percolate into the spheroids over cationic polyplexes.

i.t. distribution of polyplexes and polyplex micelles after i.t. injection

The i.t. distribution of naked pDNA, LPEI polyplexes (N/P = 6), P[Asp(DET)] polyplexes (N/P = 20), or PEG-*b*-P[Asp(DET)] polyplex micelles (N/P = 20) after the injection to solid tumors (human pancreatic adenocarcinoma BxPC3 cells) was evaluated by using Cy3-labeled pDNA (n = 3). In this experiment, each formulation was coadministered with FluoSphere fluorescent microspheres [particle size: 15 μm, 645 nm/680 nm (Ex/Em)] as a marker for the injection point. The fluorescent images of Cy3-labeled pDNA in BxPC3 tumors are shown in Figure 4a and **Supplementary Figure S2**, and the total pixels of fluorescence area and its localization in the three different regions classified by the distance from the injection point (<100 μm, 100–200 μm, >200 μm) are quantified

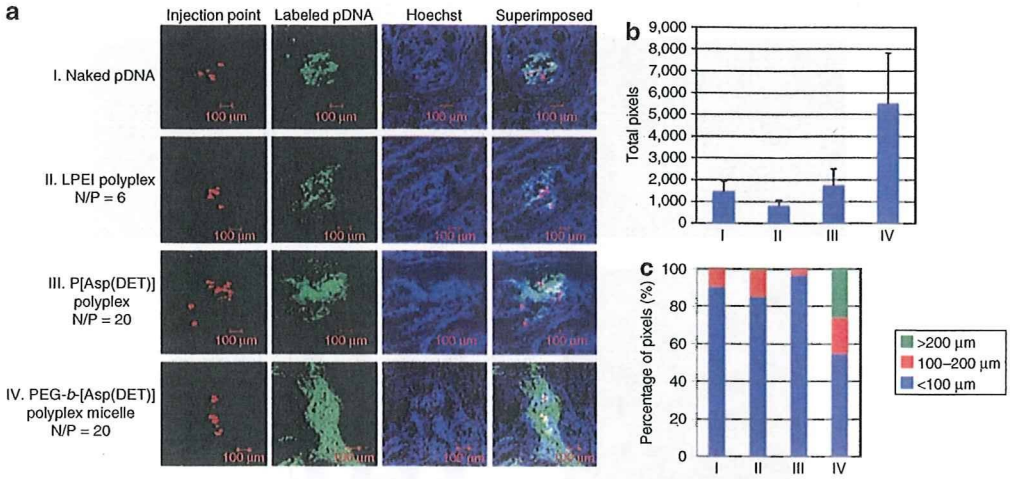

Figure 4 Intratumoral distribution of polyplexes and polyplex micelles after intratumoral injection. (**a**) Distribution of Cy3-labeled pDNA (green fluorescence) in a naked form or encapsulated into LPEI polyplexes (N/P = 6), P[Asp(DET)] polyplexes (N/P = 20), or PEG-*b*-P[Asp(DET)] polyplex micelles (N/P = 20) within human pancreatic adenocarcinoma BxPC3 tumors after intratumoral (i.t.) injection. The red and blue fluorescence are derived from fluorescent beads with a size of 15 μm as an indicator of injection point and Hoechst 33342 for the nuclear staining, respectively (more detailed data are shown in **Supplementary Figure S2**). (**b**) Total pixels and (**c**) percentage of pixels of fluorescent area of Cy3-labeled pDNA in three regions classified by the distance from the injection point. N/P, ratio of the number of amino groups units to a nucleotide unit.

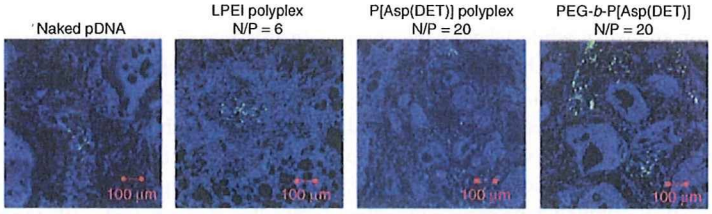

Figure 5 Gene expression of EGFP (green) within BxPC3 tumors at 6 days post-i.t. injection of naked plasmids, LPEI polyplexes (N/P = 6), P[Asp(DET)] polyplexes (N/P = 20), or PEG-b-P[Asp(DET)] polyplex micelles (N/P = 20). The blue fluorescence is derived from Hoechst 33342 for the nuclear staining. EGFP, enhanced green fluorescent protein; LPEI, linear polyethylenimine; N/P, ratio of the number of amino groups units to a nucleotide unit.

in Figure 4b,c, respectively. As a result, PEG-*b*-P[Asp(DET)] polyplex micelles showed a tendency to distribute more widely from the injection point compared with naked pDNA, LPEI and P[Asp(DET)] polyplexes. Note that irregular i.t. distribution of the polyplex micelles may be attributed to the heterogeneous structure of the BxPC3 tumors comprising clusters of dense tumor cells and interstitial tissues as indicated by the nuclear staining with Hoechst 33342.

In vivo gene expression after i.t. injection

The *in vivo* gene expression of fluorescent protein, enhanced green fluorescent protein (EGFP) within the BxPC3 tumors at 6 days post-i.t. injection of naked pDNA, LPEI polyplexes (N/P = 6), P[Asp(DET)] polyplexes (N/P = 20), or PEG-*b*-P[Asp(DET)] polyplex micelles (N/P = 20) was evaluated (n = 3). Note that P[Asp(DET)] polyplexes and polyplex micelles showed the highest transfection at 6 days postincubation in the MCTS models.[19] As shown in Figure 5, PEG-*b*-P[Asp(DET)] polyplex micelles apparently showed a widely distributed expression of EGFP in comparison with naked pDNA, LPEI, and P[Asp(DET)] polyplexes. These results seem to be consistent with the i.t. distribution of polyplex micelles (Figure 4).

Furthermore, the expression of hypoxia-responsive p5HRE + *Venus* within the BxPC3 tumors was evaluated (Figure 6a). The hypoxic region developed far from the vessels in the BxPC3 tumors was confirmed by fluorescein isothiocyanate-conjugated anti-Hypoxyprobe-1 monoclonal antibody (Figure 6b). Similar to Figure 4c, the pixels of fluorescent area in Figure 6a are classified into three different regions and summarized in Figure 6c. As a result, naked pDNA and LPEI polyplexes showed little gene expression, and P[Asp(DET)] polyplexes showed an appreciable gene expression in the region close to the injected point. In contrast, PEG-*b*-P[Asp(DET)] polyplex micelles showed well-distributed gene expression even in the furthest region from the injection point (>200 μm). These results suggest that the polyplex micelles might have the ability to percolate into the tumor tissue, thereby improving the gene transfection in the hypoxic regions of solid tumors.

DISCUSSION

Recently, we compared the transfection ability and cytotoxicity between P[Asp(DET)] polyplexes and PEG-*b*-P[Asp(DET)] polyplex micelles by using MCTS models.[19] We revealed that the PEGylation decreased the cytotoxicity of polyplexes without

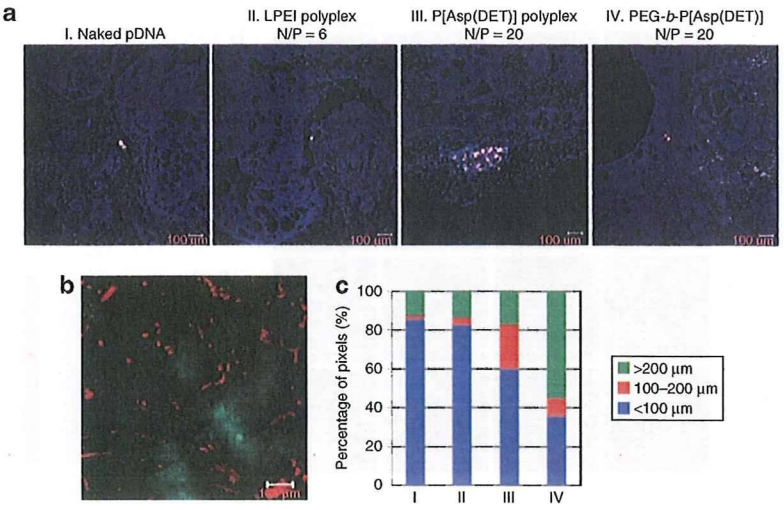

Figure 6 Hypoxia-responsive gene expression after intratumoral injection. **(a)** Gene expression of hypoxia-responsive p5HRE + *Venus* (white) within BxPC3 tumors at 6 days post-i.t. injection of naked plasmids, LPEI polyplexes (N/P = 6), P[Asp(DET)] polyplexes (N/P = 20), or PEG-b-P[Asp(DET)] polyplex micelles (N/P = 20). The red and blue fluorescence are derived from fluorescent beads with a size of 15 μm as an indicator of injection point and Hoechst 33342 for the nuclear staining, respectively. **(b)** Hypoxic regions in BxPC3 solid tumors. The red and green fluorescence are derived from anti-PECAM-1 antibody and anti-Hypoxyprobe-1 antibody, respectively. **(c)** Percentage of pixels of fluorescent area of transfected *Venus* protein in three regions classified by the distance from the injection point. i.t., intratumoral; LPEI, linear polyethylenimine; N/P, ratio of the number of amino groups units to a nucleotide unit.

compromising the transfection efficiency, while delaying the onset of gene expression. In this study, we report another important property of PEG-*b*-P[Asp(DET)] polyplex micelles, *i.e.*, tissue penetrability. We demonstrated that polyplex micelles showed facilitated percolation of loaded pDNA into the tumor tissue in both *in vitro* MCTS models and subcutaneous tumor models. Consequently, polyplex micelles showed a well-distributed gene expression after i.t. injection, allowing the transfection to the hypoxic regions of the tumors. These observations are in good agreement with our previous reports that polymeric micelles incorporating adriamycin showed enhanced percolation into the tumor tissue not only in the MCTS models[16] but also in subcutaneous tumors after intravenous administration.[17] Recently, Mellor *et al.* reported that cationic polyplexes from linear and branched PEI and lipoplexes showed penetration and transfection limited to the outer 3–5 proliferating cell layers in the large-sized MCTS (~474 nm).[11] Consistently, our results (**Figures 2b, 3d,** and **4–6**) also demonstrated not only *in vitro* but also *in vivo* that cationic polyplexes might show the limited penetration and localized transfection within the tumor. Furthermore, the result indicates for the first time that PEGylated polyplexes led loaded pDNA to show improved tissue penetrability compared with cationic polyplexes, exerting the appreciable gene expression in the inner hypoxia region.

PEGylation has apparently an advantage to prevent aggregation of polyplexes in the physiological condition with the presence of considerable amount of salt. Also, the PEGylation effectively masks the cationic nature of the core polyplexes, preventing nonspecific interaction serum proteins and extracellular matrices. Indeed, we observed that the PEG shielding of the P[Asp(DET)] polyplexes decreased the Zeta-potential from +30 mV to +6 mV. Such prevention of aggregate formation and reduced interaction with biological components by PEGylation may contribute to the facilitated percolation of the polyplexes into the tumor tissue. In this regard, the stability of polyplex micelles is an important issue during their penetration process into the tumor tissue. Our previous study revealed that the PEG-*b*-P[Asp(DET)] polyplex micelles showed much higher tolerability against the pDNA exchange reaction with an anionic lipid compared with the P[Asp(DET)] polyplexes.[19] Such increased stability of polyplex micelles is consistent with their improved penetration into the tumor tissue observed here. Furthermore, there are several reports that PEGylated nanoparticles show enhanced passage through the mucosal tissues to overcome intestinal barriers presumably due to the high flexibility and amphiphilicity of PEG chains.[21–23]

The detailed mechanisms of the enhanced percolation of polyplex micelles in the tumor tissue remain to be clarified yet; however, the results in this study clearly demonstrate that polyplex micelles might access the tumor cells in the hypoxic region with the intrinsic functions to deliver therapeutic genes. Thus, polyplex micelles are expected to treat hypoxic regions in the tumor tissue, potentially preventing the recurrence and malignant progression of solid tumors. Together with improved pharmacokinetic parameters, PEGylated polyplexes with a high tissue-percolation property might be promising nonviral vectors for *in vivo* cancer gene therapy.

MATERIALS AND METHODS

Plasmid DNA. The plasmid, pCAcc vector having CAG promoter,[24] was provided by RIKEN Bioresource Center (Ibaraki, Japan). Also, a fragment cDNA of SEYFP-F46L (*Venus*), which is a variant of yellow fluorescent protein with the mutation F46L,[25] was provided by A. Miyawaki at the Brain Science Institute, RIKEN and inserted into the pCAcc vector (pCAcc + *Venus*). Each pDNA was amplified in competent DH5α *Escherichia coli* and purified using HiSpeed Plasmid MaxiKit (Qiagen Sciences, Hilden, Germany). The plasmid, pGL5 vector having p5HRE, was provided by Faculty of Medicine, Kyoto University (Japan).[26] The DNA fragment encoding *Venus* was inserted between *Hind*III and *Xba*I sites of pGL3/5xHRE/CMVmp.

Nonviral vectors. LPEI (ExGen 500, 22 kd) was purchased from Fermentas (Burlington, Ontario, Canada). P[Asp(DET)] and PEG-*b*-P[Asp(DET)] were prepared as previously reported.[12–14] Briefly, β-benzyl-L-aspartate *N*-carboxyanhydride was polymerized by the initiation from the primary amino group of *n*-butylamine and MeO-PEG-NH_2 (M_w: 12,000) to obtain poly(β-benzyl L-aspartate) (PBLA) and PEG-*b*-PBLA, respectively. The degree of polymerization of PBLA was determined to be 98 for PBLA and 101 for PEG-*b*-PBLA by the ^{1}H NMR measurement. Then, PBLA and PEG-*b*-PBLA were reacted with diethylenetriamine (DET) (50 equiv to benzyl group of PBLA segment) under mild anhydrous conditions to obtain P[Asp(DET)] and PEG-*b*-P[Asp(DET)], respectively. The unimodal distribution and the almost 100% conversion of the BLA unit into Asp(DET) unit were confirmed by gel permeation chromatography and ^{1}H NMR measurements.

Preparation of polyplexes. Each polymer was mixed with pDNA in 10 mmol/l Tris–HCl (pH 7.4) at varying N/P ratios (final pDNA concentration: 100 μg/ml). Polyplex was applied to each well for transfection 30 minutes after preparation. Polyplex micelle was applied to each well for transfection after overnight incubation at ambient temperature.

Cell culture and preparation of MCTS. Human hepatoma HuH-7 cells (from JCRB Cell Bank, Osaka, Japan) and human pancreatic adenocarcinoma BxPC3 cells (from ATCC, Manassas, VA) were maintained in Dulbecco's modified Eagle's medium and RPMI 1640 medium, respectively, supplemented with 10% fetal bovine serum in a humidified atmosphere containing 5% CO_2 at 37 °C. MCTS were prepared by using the plate designed for spheroid formation (Sumiloncelltight; Sumitomo Bakelite, Tokyo, Japan) as reported previously.[15,18] The size of MCTS can be controlled by the incubation period. During the incubation, the medium was replaced by fresh medium containing 10% fetal bovine serum every 3 days.

Live/dead assay. Live and dead assay was accomplished with the Live/Dead kit protocol (Molecular Probes, Carlsbad, CA). MCTS was rinsed with PBS(−) and then incubated with a solution containing 0.8 μmol/l calcein AM [495 nm/515 nm (Ex/Em)] and 4 μmol/l EthD-1 (495 nm/635 nm) in PBS(−) for 3 hours at 37 °C, followed by the observation by LSM 510 confocal laser scanning microscope (CLSM) (Carl Zeiss).

Transfection to MCTS. MCTS was incubated for 6–8 days until the diameter became >400–500 μm. Then, each polyplex solution containing 1 μg pDNA was applied to each well for the transfection. After 24-hour incubation, the medium was replaced by fresh medium, followed by additional 24-hour incubation. The gene expression of the *Venus* or EGFP was then evaluated through the observation by CLSM.

Percolation of nonviral vectors into the MCTS. To visualize the distribution of nonviral vectors in MCTS, pDNA was labeled with Label IT Cy3 Labeling Kit (Mirus, Piscataway, NJ). In this experiment, MCTS with the diameter of 200–250 μm was incubated with polyplexes or polyplex micelles containing 1 μg Cy3-labeled pDNA for 24 hours. After 24-hour incubation, MCTS was harvested and rinsed, followed by observation by CLSM.

Animal models. BALB/c nude mice (female, 5 weeks old) were obtained from Charles River Laboratories (Tokyo, Japan). BxPC3 cells (5×10^6 cells in 100 μl of PBS) were injected subcutaneously into the BALB/c nude mice and allowed to grow for 2–3 weeks to reach the proliferative phase. All animal experimental protocols were performed in accordance with the policies of the Animal Ethics Committee of the University of Tokyo.

Percolation of nonviral vectors in solid tumors. After the tumor size reached 6–8 mm in a diameter, the mice received the i.t. injection of 2 μg Cy3-labeled pDNA in a naked or polyplex-encapsulated form [20 μl in 10 mmol/l HEPES buffer (pH 7.4)] by using the Hamilton Microliter Syringe (Hamilton, Reno, NV). In this experiment, 5 μl of FluoSpheres fluorescent microspheres (particle size: 15 μm, 645 nm/680 nm) were mixed with Cy3-labeled pDNA solution and simultaneously injected into the BxPC3 tumor for indication of the injection point. After 24 hours, the tumors were excised and fixed with 10% formalin and sucrose PBS(−), followed by freezing in dry-iced acetone. Frozen samples were sectioned at 10-μm thickness in a cryostat, and stained with Hoechst 33342 (Dojindo Laboratories, Tokyo, Japan). The fluorescent images were then observed by CLSM.

Transfection to solid tumors. According to the protocols for the percolation study, the tumor-bearing mice received the i.t. injection of 2 μg pCAcc + EGFP or p5HRE + *Venus* in a naked or polyplex-encapsulated form. The animals administered with pCAcc + EGFP were killed at 6 days postinjection, and the excised tumors were fixed as previously described. The fluorescence of frozen section of solid tumors was observed by CLSM. On the other hand, the animals administered with p5HRE + *Venus* were administered with Hypoxyprobe-1 (Millipore Chemicon, Billerica, MA) at 60 mg/kg via tail vein at 6 days postinjection, and then killed for removal of solid tumors. Frozen sections of the xenograft were stained with rat anti-PECAM-1 antibody (BD Pharmingen, Franklin Lakes, NJ), and subsequently stained with Alexa 594-conjugated anti-rat IgG antibody (Invitrogen Molecular Probes, Carlsbad, CA) and fluorescein isothiocyanate-conjugated anti-Hypoxyprobe-1 MAb. The section was further counter-stained with TOTO-3 (Invitrogen Molecular Probes), and the fluorescence images were captured by CLSM.

Quantitative analysis of fluorescent images. The pixels of fluorescent area of Cy3-labeled pDNA or transfected *Venus* protein in the tumor section were quantified by using the Image J software (http://rsb.info.nih.gov/ij/), and classified into three different regions by the distance from the injection point (<100 μm, 100–200 μm, >200 μm).

SUPPLEMENTARY MATERIAL

Figure S1. Distribution of labeled pDNA in BxPC3 MCTS transfected by each polyplex or polyplex micelles in intersectional profiles at the shown slices (Optical slice at the center of MCTS. Red fluorescence is Cy3 labeled-pDNA).

Figure S2. Distribution of Cy3-labeled pDNA (green fluorescence) in a naked form or encapsulated into LPEI polyplexes (N/P=6), P[Asp(DET)] polyplexes (N/P=20) or PEG-*b*-P[Asp(DET)] polyplex micelles (N/P=20) within human pancreatic adenocarcinoma BxPC3 tumors after the intratumoral injection.

ACKNOWLEDGMENTS

We thank Kotoe Date (the University of Tokyo) for technical assistance. This work was supported in part by the Core Research Program for Evolutional Science and Technology from Japan Science and Technology Agency.

REFERENCES

1. Boussif, O, Lezoualc'h, F, Zanta, MA, Mergny, MD, Scherman, D, Demeneix, B *et al.* (1995). A versatile vector for gene and oligonucleotide transfer into cells in culture and *in vivo*: polyethylenimine. *Proc Natl Acad Sci USA* **92**: 7297–7301.
2. Ogris, M and Wagner, E (2002). Targeting tumors with non-viral gene delivery systems. *Drug Discov Today* **7**: 479–485.
3. Merdan, T, Kopecek, J and Kissel, T (2002). Prospects for cationic polymers in gene and oligonucleotide therapy against cancer. *Adv Drug Deliv Rev* **54**: 715–758.
4. Pack, DW, Hoffman, AS, Pun, S and Stayton, PS (2005). Design and development of polymers for gene delivery. *Nat Rev Drug Discov* **4**: 581–593.
5. Erbacher, P, Roche, AC, Monsigny, M and Midoux, P (1995). Glycosylated polylysine/DNA complexes: gene transfer efficiency in relation with the size and the sugar substitution level of glycosylated polylysines and with the plasmid size. *Bioconjug Chem* **6**: 401–410.
6. Merdan, T, Callahan, J, Petersen, H, Kunath, K, Bakowsky, U, Kopecková, P *et al.* (2003). Pegylated polyethylenimine-Fab' antibody fragment conjugates for targeted gene delivery to human ovarian carcinoma cells. *Bioconjug Chem* **14**: 989–996.
7. Ogris, M, Brunner, S, Schüller, S, Kircheis, R and Wagner, E (1999). PEGylated DNA/transferrin-PEI complexes: reduced interaction with blood components, extended circulation in blood and potential for systemic gene delivery. *Gene Ther* **6**: 595–605.

8. Harada-Shiba, M, Yamauchi, K, Harada, A, Takamisawa, I, Shimokado, K and Kataoka, K (2002). Polyion complex micelles as vectors in gene therapy—pharmacokinetics and *in vivo* gene transfer. *Gene Ther* **9**: 407–414.
9. Jain, RK (2001). Delivery of molecular and cellular medicine to solid tumors. *Adv Drug Deliv Rev* **46**: 149–168.
10. Minchinton, AI and Tannock, IF (2006). Drug penetration in solid tumours. *Nat Rev Cancer* **6**: 583–592.
11. Mellor, HR, Davies, LA, Caspar, H, Pringle, CR, Hyde, SC, Gill, DR *et al.* (2006). Optimising non-viral gene delivery in a tumour spheroid model. *J Gene Med* **8**: 1160–1170.
12. Kanayama, N, Fukushima, S, Nishiyama, N, Itaka, K, Jang, WD, Miyata, K *et al.* (2006). A PEG-based biocompatible block catiomer with high buffering capacity for the construction of polyplex micelles showing efficient gene transfer toward primary cells. *ChemMedChem* **1**: 439–444.
13. Miyata, K, Oba, M, Nakanishi, M, Fukushima, S, Yamasaki, Y, Koyama, H *et al.* (2008). Polyplexes from poly(aspartamide) bearing 1,2-diaminoethane side chains induce pH-selective, endosomal membrane destabilization with amplified transfection and negligible cytotoxicity. *J Am Chem Soc* **130**: 16287–16294.
14. Akagi, D, Oba, M, Koyama, H, Nishiyama, N, Fukushima, S, Miyata, T *et al.* (2007). Biocompatible micellar nanovectors achieve efficient gene transfer to vascular lesions without cytotoxicity and thrombus formation. *Gene Ther* **14**: 1029–1038.
15. Itaka, K, Ohba, S, Miyata, K, Kawaguchi, H, Nakamura, K, Takato, T *et al.* (2007). Bone regeneration by regulated *in vivo* gene transfer using biocompatible polyplex nanomicelles. *Mol Ther* **15**: 1655–1662.
16. Bae, Y, Nishiyama, N, Fukushima, S, Koyama, H, Yasuhiro, M and Kataoka, K (2005). Preparation and biological characterization of polymeric micelle drug carriers with intracellular pH-triggered drug release property: tumor permeability, controlled subcellular drug distribution, and enhanced *in vivo* antitumor efficacy. *Bioconjug Chem* **16**: 122–130.
17. Kano, MR, Bae, Y, Iwata, C, Morishita, Y, Yashiro, M, Oka, M *et al.* (2007). Improvement of cancer-targeting therapy, using nanocarriers for intractable solid tumors by inhibition of TGF-beta signaling. *Proc Natl Acad Sci USA* **104**: 3460–3465.
18. Sutherland, RM (1988). Cell and environment interactions in tumor microregions: the multicell spheroid model. *Science* **240**: 177–184.
19. Han, M, Bae, Y, Nishiyama, N, Miyata, K, Oba, M and Kataoka, K (2007). Transfection study using multicellular tumor spheroids for screening non-viral polymeric gene vectors with low cytotoxicity and high transfection efficiencies. *J Control Release* **121**: 38–48.
20. An, WG, Kanekal, M, Simon, MC, Maltepe, E, Blagosklonny, MV and Neckers, LM (1998). Stabilization of wild-type p53 by hypoxia-inducible factor 1alpha. *Nature* **392**: 405–408.
21. Huang, Y, Leobandung, W, Foss, A and Peppas, NA (2000). Molecular aspects of muco- and bioadhesion: tethered structures and site-specific surfaces. *J Control Release* **65**: 63–71.
22. Samuel, KL, Elizabeth, OD, Harrold, S, Man, ST, Wang, Y, Cone, R *et al.* (2007). Rapid transport of large polymeric nanoparticles in fresh undiluted human mucus. *Proc Natl Acad Sci USA* **104**: 1482–1487.
23. Yoncheva, K, Guembe, L, Campanero, MA and Irache, JM (2007). Evaluation of bioadhesive potential and intestinal transport of pegylated poly(anhydride) nanoparticles. *Int J Pharm* **334**: 156–165.
24. Niwa, H, Yamamura, K and Miyazaki, J (1991). Efficient selection for high-expression transfectants with a novel eukaryotic vector. *Gene* **108**: 193–199.
25. Nagai, T, Ibata, K, Park, ES, Kubota, M, Mikoshiba, K and Miyawaki, A (2002). A variant of yellow fluorescent protein with fast and efficient maturation for cell-biological applications. *Nat Biotechnol* **20**: 87–90.
26. Harada, H, Kizaka-Kondoh, S and Hiraoka, M (2005). Optical imaging of tumor hypoxia and evaluation of efficacy of a hypoxia-targeting drug in living animals. *Mol Imaging* **4**: 182–193.

Cell Stem Cell

Autocrine TGF-β Signaling Maintains Tumorigenicity of Glioma-Initiating Cells through Sry-Related HMG-Box Factors

Hiroaki Ikushima,[1] Tomoki Todo,[2,3] Yasushi Ino,[2,3] Masamichi Takahashi,[2] Keiji Miyazawa,[1] and Kohei Miyazono[1,*]
[1]Department of Molecular Pathology
[2]Department of Neurosurgery
[3]Translational Research Center
Graduate School of Medicine, University of Tokyo, Tokyo 113-0033, Japan
*Correspondence: miyazono@m.u-tokyo.ac.jp
DOI 10.1016/j.stem.2009.08.018

SUMMARY

Despite aggressive surgery, radiotherapy, and chemotherapy, treatment of malignant glioma remains formidable. Although the concept of cancer stem cells reveals a new framework of cancer therapeutic strategies against malignant glioma, it remains unclear how glioma stem cells could be eradicated. Here, we demonstrate that autocrine TGF-β signaling plays an essential role in retention of stemness of glioma-initiating cells (GICs) and describe the underlying mechanism for it. TGF-β induced expression of Sox2, a stemness gene, and this induction was mediated by Sox4, a direct TGF-β target gene. Inhibitors of TGF-β signaling drastically deprived tumorigenicity of GICs by promoting their differentiation, and these effects were attenuated in GICs transduced with Sox2 or Sox4. Furthermore, GICs pretreated with TGF-β signaling inhibitor exhibited less lethal potency in intracranial transplantation assay. These results identify an essential pathway for GICs, the TGF-β-Sox4-Sox2 pathway, whose disruption would be a therapeutic strategy against gliomas.

INTRODUCTION

Glioblastoma multiforme (GBM), the most malignant form of glioma, is one of the most aggressive human cancers with a 5 year survival rate of less than one out of ten (Surawicz et al., 1998). Despite past huge efforts, this statistic has not markedly improved over the past years. Excessive proliferation, diffuse infiltration into surrounding brain tissue, and suppression of antitumor immune surveillance contribute to the malignant phenotype of glioblastomas.

Cancer-initiating cells (cancer stem cells, CSCs) are rare tumor cells characterized by their ability to induce tumorigenesis and to self-renew. Recent concepts for cancer suggest that a minority population of CSCs may determine the biological and pathological characters of tumors. Similar to other tumors, glioma-initiating cells (glioma stem cells, GSCs) have been isolated from human glioma tissues and several glioma cell lines (Singh et al., 2004; Kondo et al., 2004; Hirschmann-Jax et al., 2004). GSCs are characterized by the expression of neural stem cell (NSC) antigens and the ability to grow as nonadherent spheres termed "neurospheres" or "glioma spheres" when cultured in the presence of epidermal growth factor (EGF) and basic fibroblast growth factor (bFGF) under serum-free condition. Thus, GSCs share several characteristics with normal NSCs (Vescovi et al., 2006).

According to the concept of CSCs, failure to cure cancer may be attributed to the current therapeutic strategies, which have been aimed at the tumor bulk without significantly affecting CSCs. Like other CSCs, GSCs have been reported to be resistant to conventional radiation and pharmacological therapies (Bao et al., 2006; Liu et al., 2006a). Although elimination of CSCs has been regarded as a prerequisite for the development of successful therapeutic strategies, it has not still been fully elucidated how their stemness is maintained. To establish therapeutic strategies against glioma, in vitro and in vivo models that faithfully recapitulate the stem cell component of gliomas have been developed. Among these models, glioma spheres cultured in serum-free media supplemented with EGF and bFGF are considered to reflect biological and pathological characters of primary glioma tissues, have ability to self-renew, and mimic original tumors after intracranial transplantation (Singh et al., 2004; Lee et al., 2006).

Although transforming growth factor (TGF)-β suppresses proliferation of certain carcinoma cells and is well known to be a tumor suppressor, it promotes proliferation of tumors of non-epithelial origin, including glioma and osteosarcoma, through induction of PDGF-BB (Bruna et al., 2007; Matsuyama et al., 2003). TGF-β binds to type I and type II serine/threonine kinase receptors and transduces intracellular signals principally through Smad proteins (Derynck and Zhang, 2003; Massagué, 2008; Miyazawa et al., 2002). Upon phosphorylation by type I receptors, receptor-regulated Smads (R-Smads; Smad2 and -3) form heteromeric complexes with common-partner Smad (Co-Smad; Smad4), translocate into the nucleus, and regulate expression of various target genes. In addition to induction of proliferation, TGF-β pathway has also been implicated in invasion, metastasis, and intratumoral angiogenesis of glioma. These multiple roles of TGF-β in glioma progression have promoted the development of therapeutic agents based on the inhibition of the TGF-β pathway (Golestaneh and Mishra, 2005).

Here, we report that autocrine TGF-β signaling induces Sox2 expression, one of the crucial factors for maintenance of NSCs,

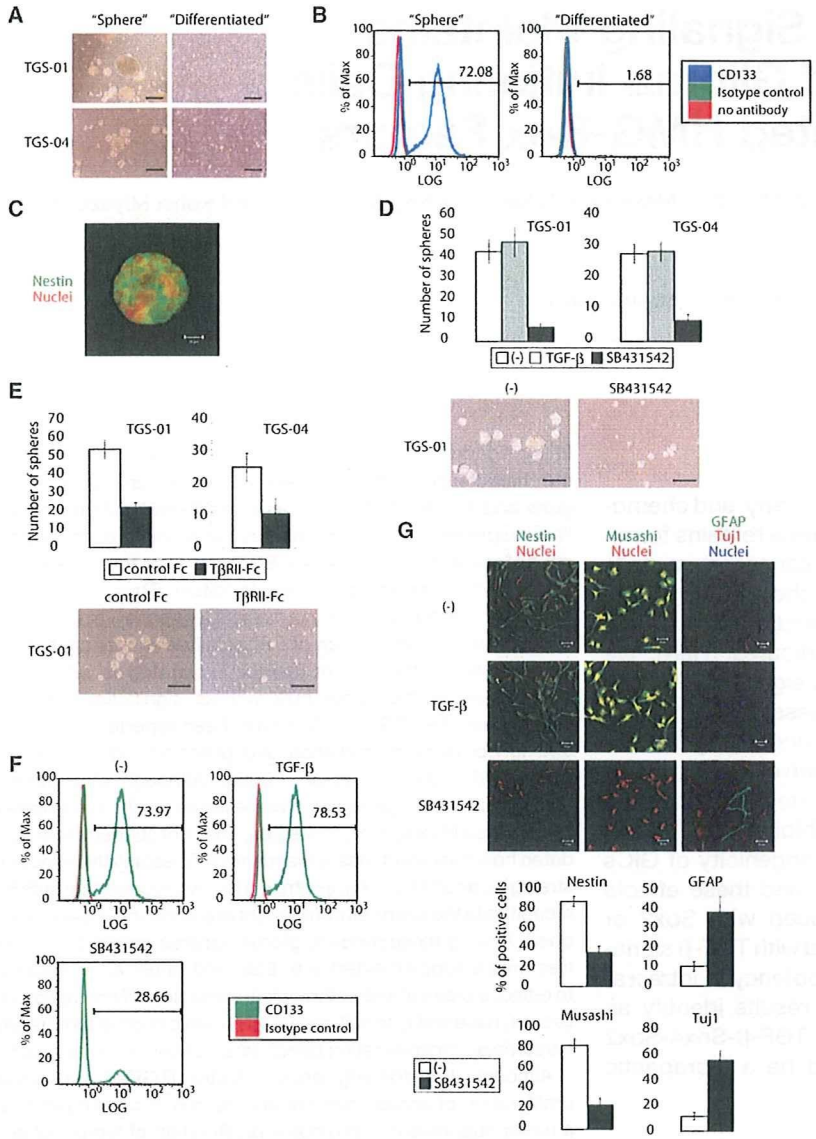

Figure 1. TGF-β Signaling Maintains Stemness of Glioma-Initiating Cells

(A) Representative images of glioma spheres TGS-01 and TGS-04 cultured in serum-free neurobasal media with EGF and bFGF ("Sphere"), and glioma cells derived from the same pathological samples as spheres but cultured in media containing 10% fetal bovine serum ("Differentiated"). Scale bars, 100 μm.

(B) $CD133^+$ ratio of "Sphere" cells (TGS-01) and "Differentiated" cells was determined by flow cytometry.

(C) TGS-01 spheres were stained with Nestin. Scale bars, 20 μm.

(D) TGF-β inhibitor deprives glioma-initiating cells of sphere-forming ability. Glioma-initiating cells were dissociated into single-cell populations and cultured with TGF-β ligand (100 pM) or inhibitor (SB431542, 1 μM) for 7 days. The data are presented as the number of glioma spheres formed (means ± SEM of five fields). Scale bars, 100 μm.

(E) Glioma-initiating cells were dissociated into single-cell populations and cultured with human TGF-β RII/Fc chimera (1 μg/ml) or control IgG_1 Fc (1 μg/ml) for 7 days. The data are presented as the number of glioma spheres formed (means ± SEM of five fields). Scale bars, 100 μm.

(F) Effects of TGF-β ligand (100 pM) or inhibitor (SB431542, 1 μM) on $CD133^+$ subpopulation of TGS-01 cells were determined by flow cytometry.

(G) Immunostaining of TGS-01 cells. Spheres were disaggregated, seeded on poly-L-ornithine and fibronectin-coated slide glasses, and cultured in serum-free medium with TGF-β ligand (100 pM) or inhibitor (SB431542, 1 μM) for 7 days. Quantification of Nestin-, Musashi-, Tuj1-, or GFAP-positive cells was shown in the bottom graphs. Scale bars, 50 μm.

and plays essential roles in maintenance of stemness of the glioma-initiating cells. We also demonstrate that another Sry-related high-mobility group (HMG) box-containing gene, Sox4, is a crucial mediator of TGF-β-induced Sox2 expression. Notably, glioma-initiating cells pretreated with TGF-β signaling inhibitor were less aggressive and showed less lethal potency in intracranial transplantation assay. These findings open the way to depriving GSCs of the tumorigenic activity and will offer new therapeutic possibilities.

RESULTS

Inhibition of TGF-β Signaling Deprives Glioma-Initiating Cells of Tumorigenic Activity

To study the mechanisms of how stemness of glioma-initiating cells is maintained, we have used glioma tissues obtained from two patients with GBM. They were cultured in serum-free medium and termed TGS-01 and TGS-04 (Figure 1A), both of which have the ability to self-renew and mimic the original tumor after transplantation into the brains of immunocompromised mice (Lee et al., 2006). Profiles of the patients and properties of the GBM cells are described in Figure S1 (in Supplemental Data available online). Expression of phosphatase and tensin homolog (Pten) was lost in TGS-01 and TGS-04 "sphere" cells. CD133 (Prominin-1) was reported to be a marker for GSCs (Singh et al., 2004). We confirmed that the $CD133^+$ subpopulation is enriched in these glioma spheres compared to cells derived from the same patient but cultured in media containing 10% fetal bovine serum ("Differentiated" or "Adherent") (Sphere; 72.0%, Differentiated; 1.6%, Figure 1B). In addition, tumor spheres derived from each of tissue samples could be passaged serially and expressed Nestin (neural precursor cell marker), confirming that these are clonogenic and self-renewing cells (Figure 1C). We also validated enrichment of glioma-initiating cells in TGS-01 and TGS-04 "sphere" cells by an intracranial transplantation assay (M.T., Y.I., and T.T., unpublished data).

To test a possible role of TGF-β signaling in glioma-initiating cells, we first examined the effect of inhibition of TGF-β signaling

on their biological characters. After treatment with TGF-β type I receptor (ALK5) kinase inhibitor SB431542 (Inman et al., 2002), glioma-initiating cells were drastically deprived of sphere-forming ability (Figure 1D). Similar results were obtained using three other glioma-initiating cells from patients with GBM (Figures S1 and S2). As SB431542 can inhibit TGF-β type I receptor (ALK5) signaling, as well as activin/nodal type I receptor (ALK4 and ALK7) signaling, we also examined the effect of TGF-β receptor II/Fc chimera (TβRII-Fc) on glioma-initiating cells to assess the role of TGF-β signaling definitely. Glioma-initiating cells treated with TβRII-Fc formed glioma spheres with lower efficiency (Figure 1E). Similar results were obtained with other TGF-β signaling inhibitors, A-78-03 (Tojo et al., 2005) or LY364947 (Sawyer et al., 2003) (Figure S3A), as well as infection of adenovirus carrying cDNA of Smad7, an endogenous negative regulator of TGF-β signaling (Figure S3B). Moreover, preformed sphere cells lost their spherical growth pattern and became attached in the presence of SB431542 (Figure S3C). Decreased number of glioma spheres formed by glioma-initiating cells with depleted TGF-β signaling suggests impaired self-renewal. In agreement with the suggested effect of TGF-β signaling depletion, treatment of glioma-initiating cells with SB431542 for 7 days prior to the sphere-forming assay without the inhibitor also reduced the number of spheres (Figure S4). We also investigated the effects of TGF-β inhibitor on the $CD133^+$ subpopulation. SB431542 decreased the size of $CD133^+$ pool in glioma-initiating cells (Figure 1F). Next, to examine the expression of neural precursor or differentiation markers in each cell, spheres in serum-free medium were disaggregated and seeded on poly-L-ornithine and fibronectin-coated slide glasses. Inhibition of TGF-β signaling decreased the number of cells positive for Nestin or Musashi (neural precursor cell markers) and increased that for GFAP (astrocyte differentiated marker) or Tuj1 (βIII-tubulin, neuronal marker) (Figure 1G). Taken together, these findings suggest endogenous TGF-β signaling maintains tumorigenicity and stemness of glioma-initiating cells. Conversely, we failed to observe striking effects of addition of TGF-β ligand on sphere-forming ability, $CD133^+$ ratio, or marker expression of glioma-initiating cells (Figures 1D, 1F, and 1G). It may be because glioma-initiating cells express all the major components of TGF-β signaling pathway and secrete TGF-β1 and -β2 proteins (Figures S5A and S5B), producing sufficient autocrine TGF-β signaling to maintain their stemness (Figure S5C).

TGF-β is reported to work as a proapoptotic or an antiapoptotic factor in a cell-context-dependent manner (Sánchez-Capelo, 2005; Ehata et al., 2007), but we failed to observe any significant effect of TGF-β ligand or inhibitor on apoptosis of glioma-initiating cells (Figure S6A). TGF-β is also known to control cell proliferation via regulating $p15^{INK4b}$, $p21^{WAF1}$, $p27^{KIP1}$, and *c-myc* (Massagué, 2008), but in glioma-initiating cells, stimulation or inhibition of TGF-β signaling did not markedly affect their expression levels at 3 or 24 hr except for only a slight increase of $p21^{WAF1}$ 24 hr after inhibition of TGF-β signaling (Figure S6B).

Sox2 Expression Is Induced by TGF-β in Glioma-Initiating Cells to Maintain Their Stemness

To elucidate the mechanism by which stemness of glioma-initiating cells is maintained by TGF-β signaling, we next examined the effect of TGF-β or SB431542 on expression of various markers for stemness. mRNA expression of Sox2, a member of HMG-box factors, was induced by TGF-β but suppressed by SB431542 after 24 hr treatment (Figure 2A) and kept at the low levels for at least 7 days (data not shown). In contrast, expression levels of Oct4, Nanog, LIF, or other pluripotent stem cell-related molecules were not significantly affected by TGF-β ligand or inhibitor in our glioma-initiating cells in TGS-01 and -04 cells (Figure S7), although Nanog and LIF were reported to be induced by TGF-β stimulation in some types of cells (Xu et al., 2008; Bruna et al., 2007). Induction of Sox2 by TGF-β was clearly suppressed in the presence of siRNA against Smad2 and Smad3 (Figure 2B), indicating that Sox2 expression is regulated by TGF-β-Smad signaling. We also confirmed regulation of Sox2 protein expression by TGF-β and SB431542 (Figure 2C). Knockdown of Sox2 expression by siRNA (Figure S8) resulted in drastic reduction of sphere-forming ability and self-renewal capacity of glioma-initiating cells (Figures 2D and 2E) and decreased size of $CD133^+$ subpopulation (75.1% to 29.3% or 35.9%; Figure 2F). Drastic reduction of sphere-forming ability by knockdown of Sox2 was also observed in four other glioma cells (Figure S9). Moreover, the number of Nestin-positive cells was reduced and that of GFAP-positive cells was increased by Sox2 knockdown (Figure 2G). These findings indicate that Sox2 is an essential factor for maintenance of stemness of glioma-initiating cells and that downregulation of Sox2 expression as early as 24 hr after treatment with SB431542 appears to be the cause, rather than the result, of deprivation of stemness of glioma-initiating cells.

Downregulation of Sox2 Is a Crucial Step for Differentiation of Glioma-Initiating Cells Induced by TGF-β Inhibitor

For further study of the role of Sox2 in maintenance of stemness by TGF-β, we examined the effect of TGF-β inhibitor on glioma-initiating cells infected with adenovirus encoding Sox2 cDNA. SB431542 only weakly deprived Sox2-overexpressed glioma-initiating cells of sphere-forming ability compared to LacZ-overexpressed cells (Figure 3A). Moreover, SB431542 failed to reduce the number of Nestin-positive cells or to increase the number of GFAP-positive cells in Sox2-overexpressed glioma-initiating cells (Figure 3B). These data suggest that deprivation of stemness of glioma-initiating cells by TGF-β inhibitor is due to downregulation of Sox2, which maintains stemness of glioma-initiating cells.

Sox4 Is a TGF-β Target Gene, which Is Highly Expressed in Glioma-Initiating Cells

Induction of Sox2 expression by TGF-β was observed 24 hr, but not 3 hr, after stimulation (Figure 2A) and attenuated in the presence of cycloheximide, an inhibitor of protein synthesis (Figure 4A). These findings indicate that Sox2 expression is not directly induced by TGF-β but regulated through other factor(s) that are induced by TGF-β. We, thus, searched candidate genes that mediate TGF-β-induced Sox2 expression to play important roles in retention of stemness of glioma-initiating cells. For this purpose, we used microarray data of public resources (Beier et al., 2007; Bruna et al., 2007; Günther et al., 2008; Lee et al., 2006; Tso et al., 2006). Criteria for selection were as follows: (1) genes with higher expression in glioma-initiating cells compared

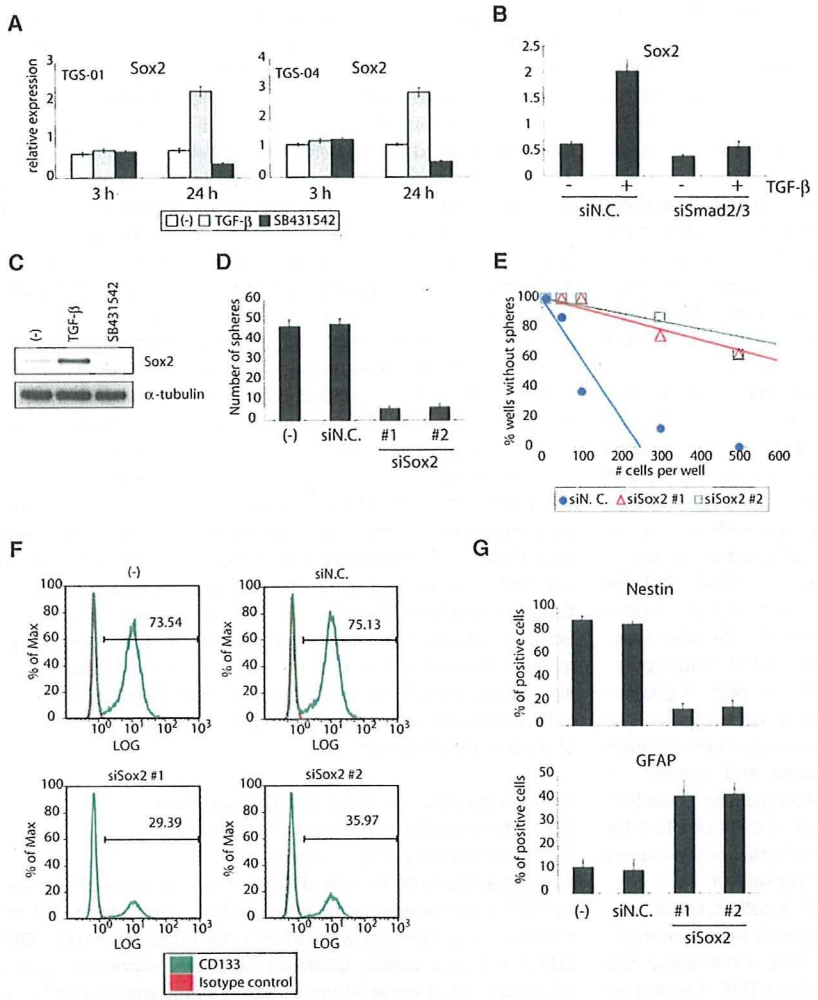

Figure 2. TGF-β Induces Expression of Sox2, an Essential Factor for Retention of Stemness of Glioma-Initiating Cells

(A) Expression of Sox2 mRNA was determined after treatment with TGF-β ligand (100 pM) or inhibitor (SB431542, 1 μM) for 3 or 24 hr. Values were normalized to that of GAPDH mRNA. Error bars represent SEM.

(B) TGS-01 cells were transfected with siRNA oligonucleotides and incubated for 24 hr. Cells were treated with TGF-β ligand (100 pM) for 24 hr. Values were normalized to that of GAPDH mRNA. Error bars represent SEM.

(C) Expression of Sox2 protein in TGS-01 cells was determined after treatment with TGF-β ligand (100 pM) or inhibitor (SB431542, 1 μM) for 24 hr. α-tubulin was used as a loading control.

(D) TGS-01 cells were dissociated into single-cell populations, transfected with control (N.C.) or Sox2 siRNA duplex, and cultured for 7 days. The data are presented as the number of glioma spheres formed (means ± SEM of five fields).

(E) Knockdown of Sox2 expression by siRNA in TGS-01 cells resulted in decrease of self-renewal capacity in limiting dilution assay.

(F) Effects of Sox2 knockdown on $CD133^+$ subpopulation of TGS-01 cells were determined by flow cytometry.

(G) Quantification of Nestin-positive or GFAP-positive cells among total cells. Differentiation of TGS-01 cells by Sox2 knockdown was analyzed 7 days after transfection of control (N.C.) or Sox2 siRNA duplex. Error bars represent SEM.

to bulk tumor cells; (2) genes directly induced by TGF-β and suppressed by TGF-β inhibitor in glioma cells; and (3) genes whose expression levels are correlated with that of Sox2 in glioma cells. Among genes highly expressed in glioma-initiating cells, we identified a transcription factor Sox4 as a TGF-β target gene.

We observed higher expression levels of Sox4 in TGS-01 and TGS-04 cells than in matched "differentiated" cells (Figure 4B). We checked whether Sox4 expression is regulated by TGF-β signaling (Figures 4C and 4D). Sox4 mRNA expression was immediately induced after TGF-β stimulation and inversely downregulated by TGF-β inhibitor in TGS-01 and TGS-04 cells. To examine whether Sox4 is a direct target gene of TGF-β, we performed chromatin immunoprecipitation assay using antibody against Smad2/3, DNA-binding mediators of TGF-β signaling. Smad complexes directly bound to Sox4 promoter in response to TGF-β stimulation, and this binding was clearly suppressed by SB431542 (Figure 4E). Moreover, induction of Sox4 by TGF-β was not significantly affected by cycloheximide (Figure 4F). These findings indicate that Sox4 is a direct target gene of TGF-β signaling.

Sox4 Associates with the Sox2 Enhancer Region and Promotes Its Expression

Next, we studied the effect of Sox4 on Sox2 expression. Sox4 overexpression in glioma-initiating cells resulted in upregulation of Sox2 expression (Figure 5A). In contrast, Sox2 expression was suppressed by Sox4 knockdown (Figure 5B). We confirmed that Sox2 mRNA expressed under the control of cytomegalovirus (CMV) promoter was not downregulated by siSox4 (Figure S10), indicating that Sox2 mRNA is not a direct target of siSox4. These results indicate that Sox2 expression is positively regulated by Sox4 at the transcriptional level. To examine whether this regulation is direct, we performed chromatin immunoprecipitation assay using antibody against Sox4. It has been demonstrated that the enhancer element located at the 3′ flanking region of Sox2 gene is important for regulation of Sox2 expression (Chew et al., 2005; Tomioka et al., 2002). The region contains the consensus binding motif for Sox4, "CATTGTA" (Liao et al., 2008). Recruitment of Sox4 to the enhancer element was increased 24 hr after TGF-β stimulation, and such recruitment was clearly suppressed by SB431542 treatment (Figure 5C). These results appear to be due to regulation of Sox4 expression by TGF-β ligand or inhibitor. In addition, TGF-β could induce Sox2 expression only weakly under the condition that Sox4 was knocked down (Figure 5D). Altogether, we concluded that Sox4 directly induced by TGF-β

upregulates Sox2 expression through association with its enhancer region.

Sox4 Is An Essential Factor for Maintenance of Stemness of Glioma-Initiating Cells

So far, Sox4 has not been reported to have any role in maintenance of stem cell properties. To study the role of Sox4 in glioma-initiating cells, we examined the effect of Sox4 knockdown on stemness of glioma-initiating cells. Sox4-knocked-down glioma-initiating cells showed less sphere-forming ability and self-renewal capacity (Figures 6A and 6B), and the size of $CD133^+$ pool was decreased (72.6% to 41.5% or 41.1%; Figure 6C). Moreover, the number of Nestin-positive cells was decreased, while that of GFAP-positive cells was increased by Sox4 knockdown (Figure 6D). These results indicate that Sox4 is involved in a crucial pathway for maintenance of stemness of glioma-initiating cells.

Sox4 Plays an Essential Role in Maintenance of Stemness of Glioma-Initiating Cells by TGF-β

From these results, we hypothesized that Sox4 expression directly induced by TGF-β promotes Sox2 expression and maintains stemness of glioma-initiating cells. To test this hypothesis, first, we examined the effect of TGF-β inhibitor on glioma-initiating cells infected with adenovirus carrying cDNA of Sox4. Sox4-overexpressing glioma-initiating cells showed resistance against deprivation of sphere-forming ability by SB431542 (Figure 7A). Moreover, the number of Nestin-positive cells and that of GFAP-positive cells of Sox4-overexpressed glioma-initiating cells were minimally affected by SB431542 (Figure 7B). These data suggest that direct induction of Sox4 expression by TGF-β plays essential roles in maintenance of stemness of glioma-initiating cells.

TGF-β Inhibitor Deprives Glioma-Initiating Cells of In Vivo Tumorigenic Activity through Downregulation of Sox4 Expression

To study the role of TGF-β-induced Sox4 in maintenance of stemness in vivo, we examined the effects of TGF-β inhibitor and Sox4 on intracranial growth of glioma-initiating cells (Figure 7C). As TGF-β is well known to promote proliferation of bulk glioma cells, SB431542 was used in pretreatment, rather than successive treatment, to distinguish the effect on differentiation from that on proliferation. The survival of the mice inoculated with SB431542-pretreated glioma-initiating cells was significantly prolonged compared to mice injected with control glioma-initiating cells. All mice bearing control glioma-initiating cells developed neurological signs and displayed large tumors. In contrast, all mice bearing SB431542-pretreated glioma-initiating cells did not develop neurological signs and the brains showed no evidence of tumor by pathological examination with H&E staining. Furthermore, the survival advantage effect of SB431542 was not observed for Sox4-transduced glioma-initiating cells (Figure 7C). Altogether, we concluded that TGF-β upregulates Sox2 expression through direct induction of Sox4 to sustain stemness of glioma-initiating cells and that TGF-β inhibitor blocks this pathway to deprive them of aggressiveness (Figure 7D).

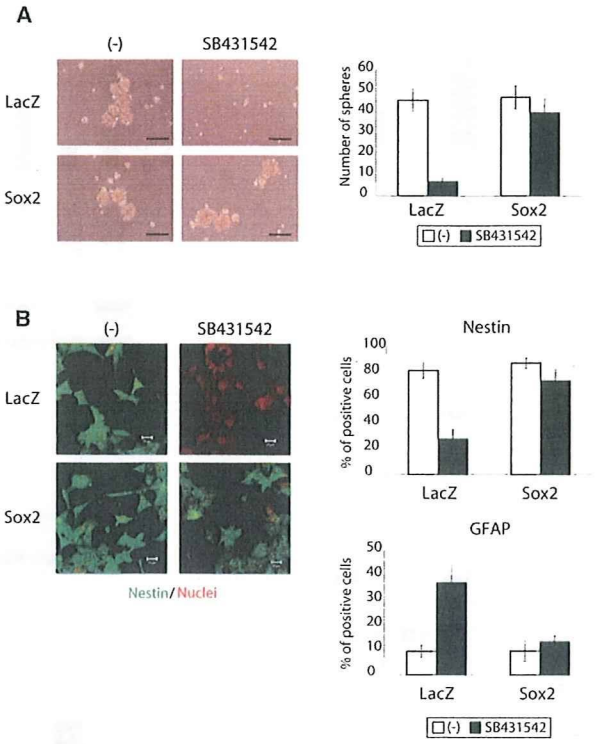

Figure 3. Downregulation of Sox2 Expression by TGF-β Inhibitor Is a Critical Step for Differentiation of Glioma-Initiating Cells

(A) Representative images of TGS-01 cells infected with adenovirus-Sox2 or LacZ (negative control) and cultured with or without SB431542 (1 μM) for 7 days. The data are presented as the number of glioma spheres formed (means ± SEM of five fields). Scale bars, 100 μm.

(B) Marker expression of TGS-01 cells infected with adenovirus-Sox2 or LacZ and cultured with or without SB431542 (1 μM) for 7 days. Images of Nestin-positive cells are shown in the left panels. Quantification of Nestin-positive or GFAP-positive cells among total cells is shown in the right graphs. Error bars represent SEM. Scale bars, 20 μm.

DISCUSSION

TGF-β was reported to induce epithelial-mesenchymal transition (EMT) in immortalized human mammary epithelial cells and increase the ability to form mammospheres (Mani et al., 2008). These findings suggest a direct link between EMT and the gain of epithelial stem cell properties of carcinoma. Such a link could be applied to other carcinoma stem cells than breast CSCs. However, since glioma cells per se have nonepithelial characters, the link may not be applied to GSCs.

To analyze roles of TGF-β signaling in glioma stem cells, we have used glioma tissues obtained from patients with GBM and they were cultured in serum-free medium ("sphere"). All of the ten mice injected intracranially with 5×10^3 TGS-01 "sphere" cells were killed within 70 days after transplantation, while all of the ten mice bearing 5×10^5 matched "differentiated" cells had survived for more than 140 days without neurological signs (M.T., Y.I., and T.T., unpublished data). These results indicate that populations with a higher tumorigenic activity were enriched in "sphere" cells.